Sizing, Operation, and Evaluation of Battery Energy Storage with Dynamic Line Rating and Deep Learning.

by

Vadim Avkhimenia

A thesis submitted in partial fulfillment of the requirements for the degree of

Master of Science

in

Software Engineering and Intelligent Systems

Department of Electrical and Computer Engineering
University of Alberta

Abstract

Integration of renewables has the potential to reduce society's reliance on carbon-based fuels. Sizing renewable-energy installations is key to making a successful business case for the construction of new assets. Dynamic thermal line rating is the amount of current in real-time that a transmission line can safely carry, and, if utilized together with utility-scale battery installations, has the potential to reduce the capacity and power rating of batteries.

Today, battery energy storage systems are operated generally with rule-based approaches where utility-scale batteries charge when they can, and discharge then they have to, or change their energy amount with the time of the day. This works aims to improve on that by introducing smart control of batteries using deep learning and deep reinforcement learning-based methods. Transmission operators today generally assume the line ampacity of the transmission lines to be stable, referred to as static line rating. Dynamic line rating, however, can be multiple times higher than static line rating, enabling the ability to sent more power accross the transmission lines.

The aim of this work is to size battery energy storage systems taking into account dynamic thermal line rating, transmission line outages, and battery degradation, and explore decentralized control of batteries. A combination of non-linear programming for battery action prediction is used together with deep learning-based forecasting of ampacity and load. The approach is tested on IEEE 24-bus test grid. A deep reinforcement learning-based approach is utilized to predict battery actions, and test it on IEEE 6-bus test grid. A method for evaluating battery capacity and power rating sizes based on comparing the selection criteria with the allowed tolerance in

unserved energy, unserved energy duration, and the number of unserved energy events is presented. A method to generate synthetic 100-step time series of Alberta electricity pool prices and dynamic thermal line rating is demonstrated, that can be used to supplement existing data sets, and be applied in reinforcement-learning simulations.

Preface

This is original work by Vadim Avkhimenia, under the superbvision of Dr. Petr Musilek and Dr. Tim Weis, with the help of Dr. Matheus Gemignani. This work is based on the papers "Generation of Synthetic Ampacity and Electricity Pool Prices using Generative Adversarial Networks" presented at 2021 IEEE Electrical Power and Energy Conference, "Sizing Transmission-Scale Battery Energy Storage System with Dynamic Thermal Line Rating" presented at the 2022 IEEE Power and Energy Society General Meeting, "Deep Learning Control of Transmission System with Battery Storage and Dynamic Line Rating" to be presented at the 2022 IEEE Sustainable Power and Energy Conference, "Deep Reinforcement Learning Operation of Battery Storage with Dynamic Line Rating" to be submitted, and "Sizing and Evaluation of Battery Energy Storage System in Transmission Systems with Dynamic Thermal Line Rating", to be submitted.

"If it was hard everyone would do it."

- Anonymous

To my parents and my wife.

Acknowledgments

I would like to thank my supervisors, Dr. Petr Musilek and Dr. Tim Weis, for supporting me at every stage of this research. I would also like to thank the former director of the University of Alberta's CABREE group, Dr. Andew Leach, for his useful guidance in regards to the technical aspects of linear programming. I would like to thank my co-author Dr. Matheus Gemignani for continuously supporting my efforts. I would like thank Dr. Akhtar Hussain for providing me with countless useful instructions in optimization and algorithms. I would also like to thank my colleagues in the ENTAIL group, Dr. Mohammed Al-Saffar, Peter Atrazhev, Daniel May, Chloe Zhou, Nastaran Gholizadeh, Amirhossein Sohrabbeig, Mikael Sabuhi, and Stephen Fan for all the help they provided me. Finally, I would like to thank my parents and my wife, for helping me emotionally throughout this journey.

Table of Contents

List of Tables

List of Figures

Abbreviations & Acronyms

AESO Alberta Electric System Operator.

BADC British Atmospheric Data Center.

BESS Battery Energy Storage System.

CNN-biLSTM Convolutional Neural Network bi-directional Long-Short Term Memory.

DDPG Deep Deterministic Policy Gradient.

DL Deep Learning.

DOD Depth of Discharge.

DRL Deep Reinforcement Learning.

DTLR Dynamic Thermal Line Rating.

LSTM Long-short Term Memory.

MADDPG Multi-agent Deep Deterministic Policy Gradient.

MAPE Mean Average Percentage Error.

MASAC Multi-agent Soft Actor Critic.

MILP Mixed-integer Linear Programming.

MLP Multi-layer Perceptron.

MMD Maximum Mean Discrepancy.

MSE Mean Squared Error.

MW Mega Watt.

MWh Mega Watt Hour.

NLP Non-linear Programming.

NMC Lithium Nickel Manganese Cobalt.

PCA Principal Component Analysis.

PINN Physics-Informed Neural Network.

RTS Reliability Test System.

SAC Soft Actor Critic.

SLR Static Line Rating.

SOC State of Charge.

SOH State of Health.

TRTR Train Real Test Real.

TRTS Train Real Test Synthetic.

TSTR Train Synthetic Test Real.

TSTS Train Synthetic Test Synthetic.

WGAN Wasserstein Generative Adversarial Network.

WGAN-GP Wasserstein Generative Adversarial Network Gradient Penalty.

Chapter 1

Introduction

Transmission line outages in multi-bus transmission systems may prevent loads from being served at the substations. To alleviate this problem, a battery energy storage system installed in certain locations in the network can supply the necessary power to prevent unserved loads from appearing. Power flow across the transmission line is limited by the rating of that line in Amperes. If the rating of the line is insufficient, in certain cases power may not be able to travel to the required substations. Transmission utility companies typically keep the amperage ratings of the transmission lines constant for reliability reasons, referred to as static line rating. However, the ampacity of the transmission lines varies with ambient temperature, wind speed, wind direction, and solar irradiance. Variable ampacity of the lines, also called dynamic thermal line rating, can be multiple times higher than its static counterpart, and if dynamic thermal line rating is used instead of static line rating, in some cases, a higher amount of power may be allowed to flow across the transmission line, alleviating unserved load. This work explores using battery energy storage systems and dynamic thermal line rating in combination, to alleviate unserved load at substations.

The motivation of this work is to understand how to size and evaluate battery energy storage system capacity and power rating taking into account dynamic line rating, transmission line outages, and battery energy storage system degradation. Additionally, the work should explore battery energy storage system control using

modern artificial intelligence approaches.

The specific objectives of this work are:

1. Develop a method to generate multi-time step synthetic sequences of ampacity and electricity pool price data that can later be used for simulations and model training.

2. Design a BESS sizing methodology considering DTLR, BESS degradation, transmission line outages, and multi-year operation and evaluate the effectiveness of BESS capacity and power rating.

3. Use load and ampacity forecasts to predict BESS behavior.

4. Apply modern control algorithms in a multi-bus system to predict BESS action.

The work to address objective 1 was published in "Generation of Synthetic Ampacity and Electricity Pool Prices using Generative Adversarial Networks" paper presented at the 2021 IEEE Electrical Power and Energy Conference (EPEC). Work in "Sizing Transmission-Scale Battery Energy Storage System with Dynamic Thermal Line Rating" addressed objective 2 and was presented at the 2022 IEEE Power and Energy Society General Meeting (PES GM). Additionally, objective 2 will be addressed in the paper titled "Sizing and Evaluation of Battery Energy Storage System in Transmission Systems with Dynamic Thermal Line Rating", which is yet to be submitted for publication. Objective 3 was addressed in "Deep Learning Control of Transmission System with Battery Storage and Dynamic Line Rating", which will be presented at the 2022 IEEE Sustainable Power and Energy Conference (iSPEC). Objective 4 will be addressed in the paper "Deep Reinforcement Learning Operation of Battery Storage with Dynamic Line Rating", also yet to be submitted for publication.

The five papers share in common the battery sizing methodology. This methodology is largely repeated in the introductory section of every paper.

Chapter 2

Background

2.1 Synthetic Ampacity and Electricity Prices Data Generation

In order to train reinforcement learning and deep learning models massive amounts of data is often needed, sometimes more than is available. For this reason we explore the different methods of generating synthetic data, in particular, by applying Generative Adversarial Networks. The background for this is presented in Section 3.2.

2.2 BESS Capacity Sizing and Capacity Evaluation

Before a battery energy storage system can be operated, it needs to be sized. The different methods that were recently used to size the battery capacity and battery power rating were explored. The background is presented in Sections 4.2 and 7.2.

2.3 Deep Learning BESS Control

Decentralized control of battery energy storage can be difficult. Here we present the different methods used recently to control batteries in transmission and distribution systems. We focus here on the applications of Deep Learning to enable battery control by forecasting load and ampacity. The background is presented in Section 5.2.

2.4 Deep Reinforcement Learning Control

Deep Reinforcement Learning presents a natural approach to control multiple batteries by allowing the discovery of optimal policies for the operation of batteries. We focus here on algorithms that use continuous state and action spaces. The background is presented in Section 6.2.4.

Chapter 3

Synthetic Dynamic Line Rating and Electricity Prices Generation for Simulations

3.1 Introduction

Availability of data for training deep learning and reinforcement learning models can be a challenge in cases where data privacy and scale of data do not allow large volumes of data to be stored [1]. Additionally, some datasets rely on experts to design, which limits the amount of data in the datasets [2]. For simulations and scenario planning involving dynamic thermal line rating (DTLR), the privacy and scale, and for simulations with pool price data. the scale, may present an issue.

A natural way to supplement existing data is to create synthetic datasets. Synthetic DTLR and AESO pool price data can be used to simulate Alberta grid operations. In this work we attempt to create synthetic data samples based on DTLR and AESO pool price data by employing a generative adversarial network (GAN) to learn the probability distribution of the real data. GANs work by sampling noise from a normal distribution and use that noise as inputs into a generator neural network to generate realistic samples of data. The discriminator neural network is then fed the generated samples and the real samples of data to try to distinguish the two, thereby training both the generator and discriminator until the desired performance of the generator

is achieved [3].

The ability of transmission lines to carry large amount of current through them is limited by the maximum temperature of the conductor. This temperature limit directly determines the maximum amount of current that can pass through the transmission line. For ease of planning the maximum current a transmission line is rated for is fixed and this referred to as the Static Line Rating (SLR) measured in Amperes. However, solar irradiance, wind speed, rainfall, wind direction and ambient temperature all affect the temperature of the conductor. Based on these values a real-time DTLR of the transmission line can be determined, eg., using the IEEE-738 standard [4]. DTLR can impact operational decisions that affect the flow of power transmitted. In Alberta, the system marginal price (SMP) of power is determined based on the price of power blocks offered into the AESO Energy Trading System and the Alberta Internal Load. The hourly weighted average of SMP determines the hourly pool price [5]. The hourly prices generators are paid for their delivered energy in Alberta's competitive energy market are based on the pool price and may impact the costs of generators and transmission operators.

As part of our reliability study, samples of DTLR and AESO pool price data are necessary to train a reinforcement learning (RL) agent using the environment which can be used to simulate real-world conditions by drawing time-series samples of DTLR and pool price data. Once the samples are drawn, an RL agent can go forward in time, using the synthetic samples to calculate the earned rewards and learn the necessarily policy utilizing any of the popular RL algorithms [6], [7]. These samples can be obtained from historical data. However, situations when DTLR is less than SLR are infrequent and conditions responsible for the AESO pool prices may influence the DTLR. Additionally, our work involves forecasting DTLR based on historical DTLR data [8]. To improve existing DTLR forecasting models the existing dataset can be augmented by including supplemental data, not part of the original dataset, which can then be used in conjunction with existing data to train the models [9].

Large number of DTLR and AESO pool price samples can be obtained by synthesizing DTLR data based on the statistics of the historical data. An attempt at using convolutional neural network (CNN) architectures in the generator and discriminator for the generation of synthetic DTLR and AESO pool price data yielded poor results, as evaluated using a visual inspection of the synthetic data, the resulting principal component analysis (PCA) plots, and the resulting frequency distribution of the synthetic data. The synthetic data generated also suffered from mode collapse [10] which suggested the use of Wasserstein GAN (WGAN) architecture to enable the GAN to learn the distribution of the real data. 100-step samples were chosen for each dataset not to overwhelm the training of the GANs. The use of WGAN architecture resulted in data samples that had a strong overlap in the PCA decomposition between the real data and the synthetic data, a stable maximum mean discrepancy loss (MMD), good visual appeal, and a regression error on the same order of magnitude when training the regression model on the real data and testing it on the synthetic data.

This article is organized in 6 sections. Section 3.2 describes the recent progress in the synthetic generation of data using GANs. The structure and evaluation methods of GANs are explained in section 3.3. Information about the datasets used and the neural network architecture of WGAN are documented in section 3.4. Section 3.5 evaluates the performance of WGAN in generating synthetic data. The results are summarized in section 3.6 and the supporting figures are presented in the Appendix.

3.2 Related Work

Synthetic time-series data has recently been successfully produced using GANs. For exmaple, in healthcare, recurrent conditional GANs (RCGAN) were used for the generation of realistic intensive care unit patient data [11]. RCGAN uses Long Short Term Memory (LSTM) cells in the generator and discriminator to introduce memory into the networks. Harada et al. explored the generation of bio-signal data and the relationship between the distribution of the latent variables and the output variables

as canonical loadings via the canonical correlation analysis (CCA) [12]. The authors show that the CCA of the latent variables can be used to control the characteristics of the synthetic data and use deep LSTM as part of the architectures of the generator and discriminator. Zhu et al. [13] explored the generation of synthetic electrocardiogram data utilizing convolutional bidirectional LSTM GAN (biLSTM-CNN GAN) with the generator architecture using 2 biLSTM layers and discriminator architecture using the CNN layers. This was found to outperform Recurrent Neural Network Autoencoder (RNN AE) and RNN Variational Autoencoder (RNN VAE) architectures. GANs were also useful in generating synthetic brain signals. Electroencephalographic (EEG) brain signals are synthesized using EEG-GAN which uses convolutional neural networks (CNNs) involving up-sampling and down-sampling to improve the generating ability of the generator [14]. The generation of synthetic electroencephalogram signals using CNN GAN is also explored in [15]. Electrocardiogram (ECG), electroencephalogram (EEG), electromyography (EMG), photoplethysmography (PPG) biomedical health data is generated using SynSigGAN which uses bidirectional grid LSTM in the generator architecture and CNN for the discriminator architecture [2].

In financial analysis, Quant GAN uses temporal convolutional networks which allow for the capture of volatility clusters and the generation of S&P 500 index prices [16], while Fu et al. used conditional GANs (CGANs) to simulate heavy-tailed distributions for applications in financial counter-party risk analysis [17]. TimeGAN introduced an embedding space which was jointly optimized to capture the temporal correlations of data and outperformed RCGAN on stocks and energy datasets [18].

Synthetic data was generated to aid simulations in smart grids and automotive applications. Deep convolutional architectures were used in the generator and discriminator of the conditional GAN to create synthetic data for the solar generation and load consumption which was shown to perform well on the MMD loss and TRTS/TSTR [19]. Multi-conditional GAN (MCGAN) were supplemented with extendible conditions via input tensors to synthesize parking data [1]. An unlabeled dataset of

in-vehicle signals was created using a Variational Autoencoder GAN (VAE GAN) architecture [20].

Wasserstein GANs (WGANs) introduced an improvement to training GANs by attempting to eliminate mode collapse in the distribution of the generated data [21]. WGANs make use of the Wasserstein distance metric, also known as the earth-mover distance as the objective function to be minimized and clip the weights of the networks to be within the specified range to introduce stability during training. Time-series GAN (TSGAN) uses two WGANs in tandem to generate time-series data and was shown to outperform WGANs on 70 datasets with the Frechet Inception Score (FID) as the metric [22]. TSGAN was then improved by introducing unified TS-GAN (uTSGAN) by combining learning and training [23]. WGANs were integrated with graded sequences of statistics, called path signatures, which described the data stream. The discriminator was based on a new sig-W_1 metric, which captured the joint distribution of time series, thereby reducing the need for extensive training [24]. Financial stock-price data was synthesized successfully using WGAN with Gradient Penalty (WGAN-GP) [10], [25].

Building on previous work, this work introduces a convolutional WGAN architecture for the generation of DTLR and pool price data that does not suffer from mode collapse and results in realistic-looking synthetic time-series.

3.3 Methodology

3.3.1 Generative Adversarial Networks

GANs are neural network architectures where one neural network, the generator, G, generates synthetic data, based on a prior normal distribution, $p_z(z)$, and the second neural network, the discriminator, D, tries to distinguish the generated data from the real data [3]. The competing networks are involved in a minimax contest with the generator attempting to fool the discriminator by generating realistic data compared

with the real data used for training. The generator is attempting to capture the distribution of the real data, i.e. $G(z) \sim p_{data}(x)$. The value function $V(G, D)$ is

$$\min_G \max_D V(G, D) = \mathbb{E}_{x \sim p_{data}(x)}[\log(D(x))] - \mathbb{E}_{z \sim p_z(z)}[\log(1 - D(G(z)))]. \tag{3.1}$$

Intuitively the generator tries to fool the discriminator thereby minimizing the loss function while the discriminator tries to maximize it. Mode collapse is a condition that occurs when the generator is able to capture only a few modes of the distribution, while missing the rest, which results in synthetic distribution being different from real data distribution and poor synthetic data. To counter mode collapse, Wasserstein GAN architecture is used [10], which was shown to be effective for preventing mode collapse via using the earth-mover distance as the objective function [21].

3.3.2 Wasserstein GAN

In WGAN, the objective function is the Wasserstein distance W between two distributions, $p_{data}(x)$ and $G(z)$, which is the smallest distance between the two distributions, defined as

$$W(p_{data}, p_z) = \max_w \mathbb{E}_{x \sim p_{data}(x)}[f_w(x)] - \mathbb{E}_{z \sim p_z(z)}[f_w(G(z))], \tag{3.2}$$

where f_w is a Lipschitz function which can be approximated by a deep neural network. The function outputs a score that represents the degree to which the discriminator believes the samples are real. The discriminator is then called the critic. To improve training, weights of the parametrized function f_w are clipped to be within specified values $[-c, c]$, where c is a hyperparameter for the network architecture [10].

3.3.3 Evaluation Criteria

Evaluating the performance of GANs on a dataset can be challenging. To show that synthetic and real data are indistinguishable, statistical tests need to be performed [1].

We apply PCA to visually compare the 2-dimensional decomposition of the real and synthetic datasets [18]. Better results mean two plots overlapping closely.

In Train Real Test Synthetic (TRTS), a prediction regression model is trained on samples of real data. The trained model is then used on a sample of synthetic data to make a prediction and the performance of the model is measured [18]. This performance is compared against the performance of the model on the sample of real data that the model has never seen before. A common metric used is mean absolute percentage error [1]. The aim is to have the two performance metrics close to each other. Similarly, the quality of the synthetic data can be evaluated by training a regression model on a sample of synthetic data and comparing its performance on a sample of real data. A 2-layer deep neural network consisting of 2 LSTM layers, each with 100 cells, is used for regression. 95% of sample length is used for training and 5% for evaluation. The results are averaged over 30 iterations.

A qualitative assessment of the frequency histogram of the real data compared against the synthetic data provides a visual assessment of the distribution of synthetic data [10]. Maximum mean discrepancy (MMD) loss can be used to measure the distance between the different distributions [26]. However, training the GAN longer does not guarantee that the generator will perform better. In this study $\{x_i\}_{i=1}^{N} \sim p(x)$ and $\{y_j\}_{j=1}^{M} \sim q(y)$, the MMD estimate is calculated from [1]

$$MMD^2 = \frac{1}{N^2}\sum_{i=1}^{N}\sum_{j=1}^{N} K(x_i, x_j) + \frac{1}{M^2}\sum_{i=1}^{M}\sum_{j=1}^{M} K(y_i, y_j) - \frac{2}{NM}\sum_{i=1}^{N}\sum_{j=1}^{M} K(x_i, y_j), \tag{3.3}$$

with the radial basis function kernel K calculated as

$$K(x, y) = \exp(-||x - y||^2/(2\sigma^2)), \tag{3.4}$$

where σ is a hyper-parameter.

3.4 Dataset and Architecture

3.4.1 Dataset

The DTLR dataset was provided by a transmission facilities operator (TFO) in Alberta, Canada. It consists of 1-minute interval DTLR readings which span between January 1, 2018 and January 1, 2019. The DTLR measurements were calculated based on the weather conditions recorded by the nearby weather station and translated into DTLR values using the IEEE-738 standard [4]. The AESO power pool dataset was collected using AESO Energy Trading System (ETS) records [5]. Hourly power pool data span from January 1, 2020 to January 1, 2021, and are presented in dollars per megawatt hour ($/MWh). Both datasets were standardized and then normalized to values between -1 and 1 to bound the f_w [21] and to speed up computation [27].

3.4.2 Architecture

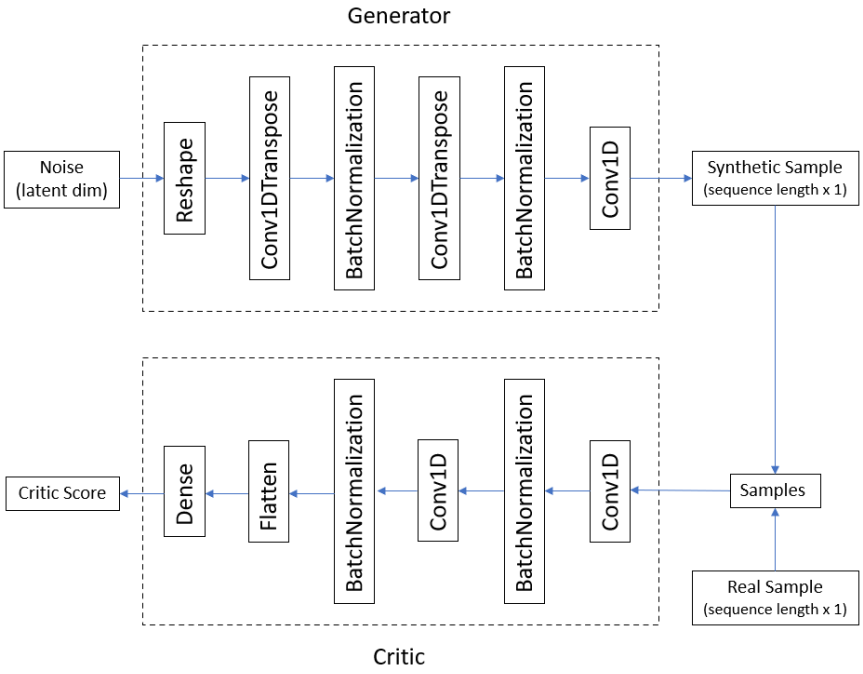

Figure 3.1: WGAN Architecture.

Keras wrapper was used to construct the neural networks [28]. The architecture of the generator consists of the layers added in sequence, starting with and input with

Table 3.1: Performance on Dataset

Dataset	***TRTS***	***TSTR***	***TRTR***	***TSTS***
DTLR	6.3%	9.2%	7.7%	5.2%
AESO	16.8%	14.8%	17.5%	9.8%

the size of the latent dimension [29]. In both the generator and the critic architecture following every dense layer and every batch normalization layer was a leaky ReLU layer with $\alpha = 0.2$, except for the output of the critic. The architecture is shown in Figure 3.1. The weights of the neural network were clipped with $c = 0.01$ as recommended in [21]. Learning rate of 0.00005 was used together with RMSProp optimizer. The critic was trained 5 times for every time the generator was trained.

3.5 Results

The maximum and minimum values of synthetic DTLR data of 2667.61 A and 414.51 A, lie within the maximum and minimum value range of 2811.7 A and 383.9 A, the latter corresponding to real data. For the pool price dataset the maximums of both synthetic and real data are 999.99 $/MWh and the minimum of 0.09 $/MWh for synthetic data is close to the minimum of 0 $/MWh for real data. For both DTLR and AESO pool price datasets it can be seen from Figure 3.8 that the MMD loss stabilizes after 9000 epochs, and therefore the best models lie at epochs value above that. Visual inspections of the frequency density distributions of the synthetic samples compared to real, shown in Figures 3.2 and 3.3, and the PCA decomposition of the synthetic and real data, shown in Figures 3.4 and 3.5, identify the correct models. Visual inspections of the samples of synthetic data compared with the real data is then performed to inspect the synthetic datasets. The synthetic data shown in Figure 3.6 and Figure 3.7 indicate a close resemblance. The TSTR results from Table 3.1 show that for DTLR dataset, training the LSTM models on the real data

and testing it on synthetic data produces an error of 6.3%, which is similar to the 7.7% error obtained when testing the models on real data. Error of 9.2% is obtained when the models are trained on synthetic data and tested on the real dataset. For AESO pool price dataset the TRTS results in an error of 16.8% against the error of 17.5% when testing with real data. TSTR results in an error of 14.8% against the error 9.8% when testing with synthetic data. The mean absolute percentage error results agree well within 4% for the DTLR dataset and within 5% for the AESO pool price dataset, when trained on synthetic data and tested on real data, indicating good GAN performance.

Generated synthetic data can then be used to perform simulations, such as simulating the environment for RL agents and to train forecasting models, as has been demonstrated by the performance on the TSTS metric, The availability of synthetic data can also be used in applications involving mixed-integer linear programming to obtain better average values and verify extracted values.

3.6 Conclusion

Increasing the number of samples in and quality of datasets that can be used in smart grid applications can improve the quality of existing machine learning models in practical applications. Using WGAN we generated synthetic DTLR and AESO pool price data with similar frequency distributions and PCA decomposition as the real data. The WGAN was shown to generate realistic-looking DTLR and AESO pool price data with 100 time-step durations. Statistical tests showed that the synthetic data shares key properties with real data. Future work can involve an improvement in WGAN architecture using RNNs to increase the predictive accuracy over the TRTS metric. The sequence length of the generated data can be increased enabling applications over longer time horizons. The existing WGAN can be conditioned on average ambient temperature, wind speed, wind direction, and solar irradiance numerical range classes to generate synthetic DTLR and pool price data specific to those average ranges.

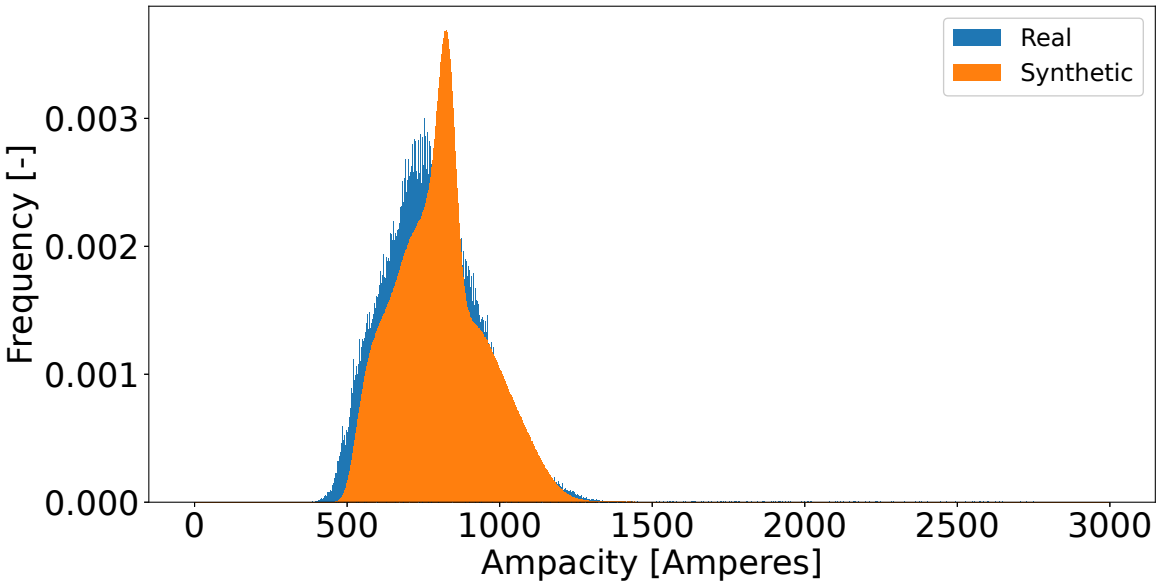

Figure 3.2: Synthetic and real data distribution for 100 time step samples for DTLR dataset.

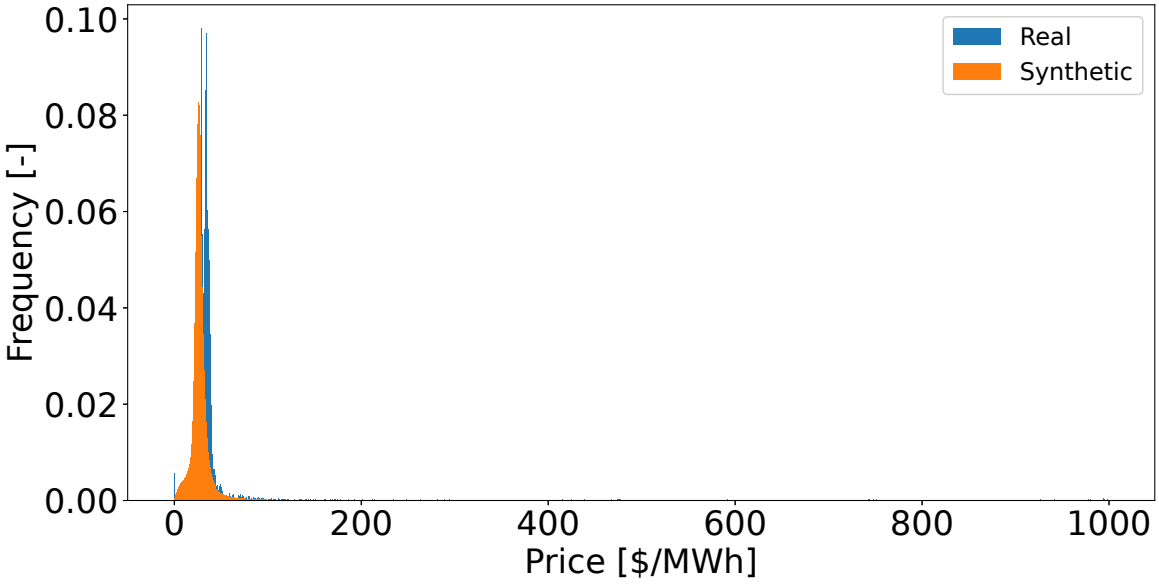

Figure 3.3: Synthetic and real data distribution for 100 time step samples for market pool price.

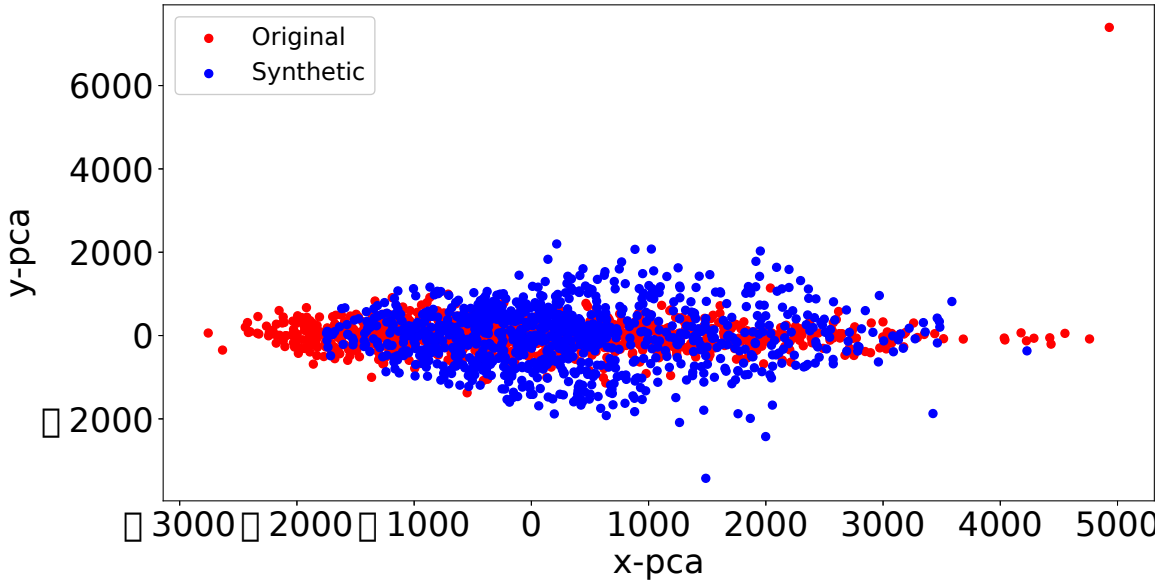

Figure 3.4: PCA decomposition for real data and synthetic data for DTLR dataset.

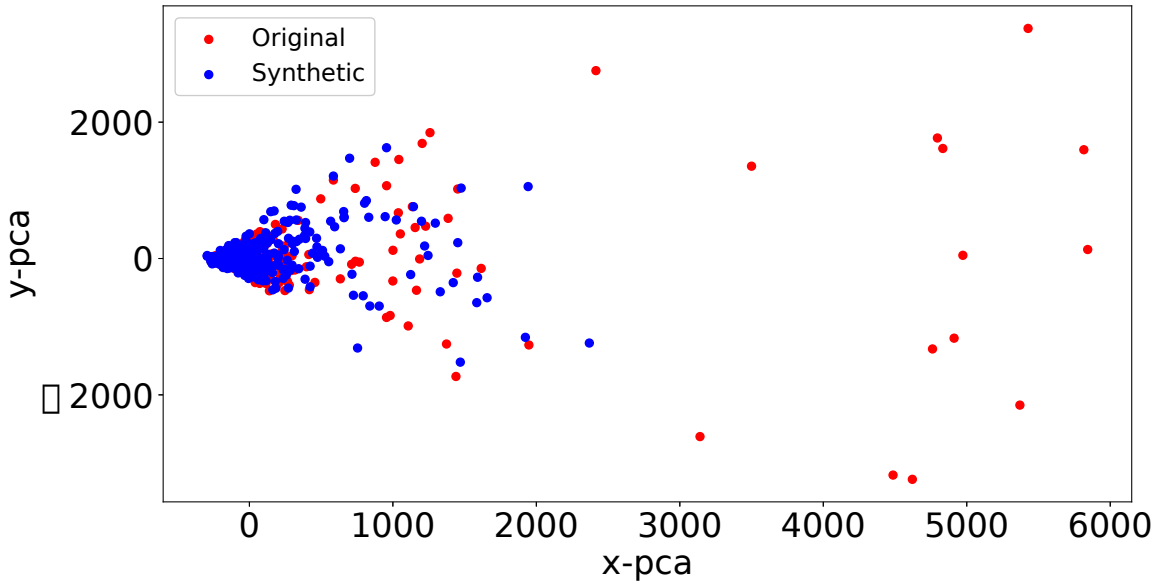

Figure 3.5: PCA decomposition for real data and synthetic data for market pool price.

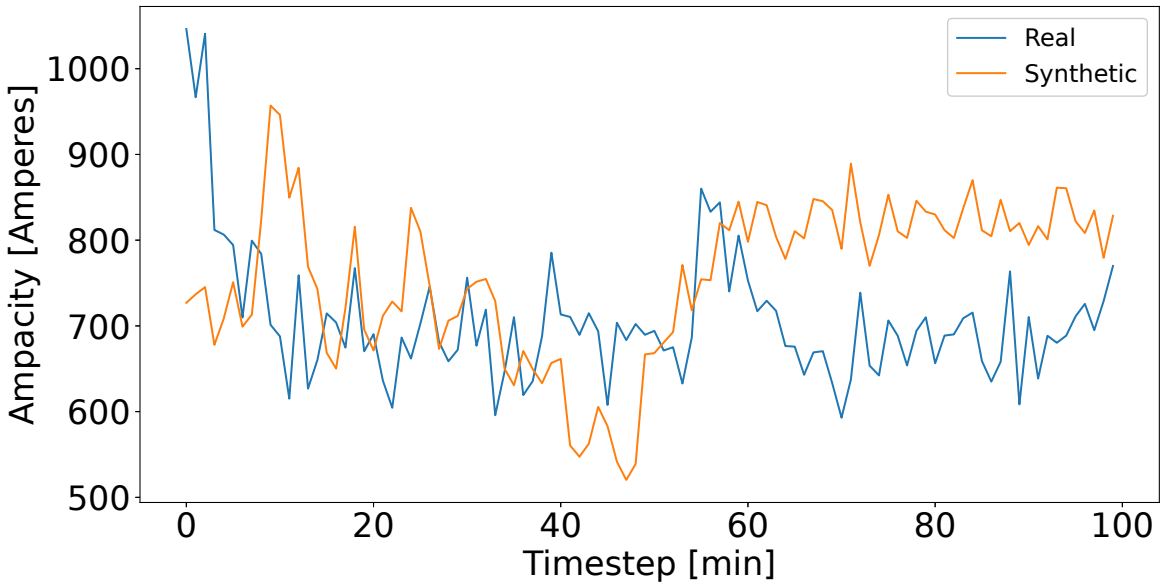

Figure 3.6: Synthetic data generated for DTLR dataset.

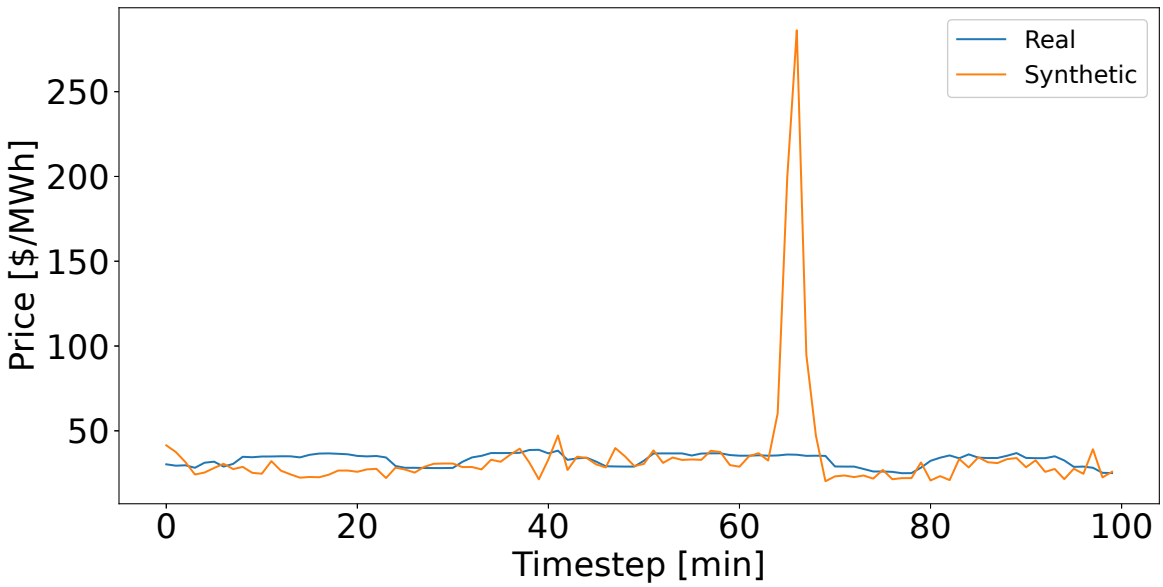

Figure 3.7: Synthetic data generated for market pool price.

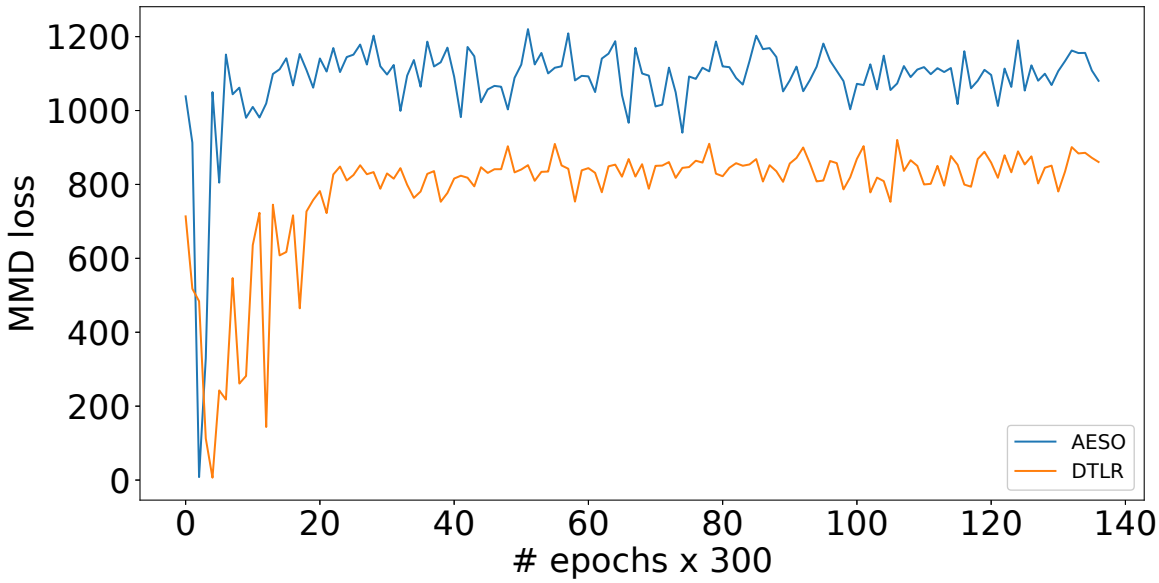

Figure 3.8: MMD loss for 100 time step runs.

Chapter 4

BESS Capacity Sizing

4.1 Introduction

Power grids are built considering worst case demand and generation scenarios [30]. Building new components, such as new transmission lines and generators, to satisfy the low probability realistic worst-case scenarios is necessary but expensive. Schemes to reduce the impact of peak demand include time-of-use energy pricing, demand response, battery energy storage system (BESS) installations, bidirectional vehicle-to-grid power supply, and implementing dynamic thermal line rating into operations. Building new BESS installations and the use of dynamic thermal line rating are two ways grid operators can control the impact of high demand on the grid, thereby reducing the costs associated with new installations [31]. This work explores the use of the two technologies in combination.

The ability of transmission lines to carry power is limited by the internal conductor temperature [32]. This temperature is influenced by ambient temperature, wind speed, wind direction, and solar irradiation. The amount of current a transmission line can carry, its ampacity (also known as dynamic thermal line rating, DTLR), thus varies dynamically with the environmental conditions. For ease of planning and safety of equipment, the amount of current a transmission line can carry is assumed to be constant and is known as static line rating (SLR) [33]. SLR values are chosen conservatively to ensure that the ampacity is rarely below the SLR. In practice,

ampacity can be multiple times higher than SLR, which means that in some cases existing transmission lines can carry higher power without needing any upgrades or new transmission lines being built. Furthermore, BESS positioned near a substation can discharge its energy to alleviate the load at the substation, thereby requiring less power to be supplied via the transmission lines and extending their operating range beyond SLR. The two technologies can act together in tandem to reduce the need for the construction of new transmission lines [34]. It is therefore useful to properly size the BESS capacity and BESS power rating.

When sizing BESS for interconnected systems, the effect of transmission line outages and BESS degradation are important. Transmission line outages force the power to be rerouted around the affected transmission lines, causing an increase in the required BESS capacity. BESS degradation depends on the self-discharging behavior of the BESS as well as on the amount of cycling the BESS is undergoing. While the former process is inevitable, the latter can be reduced via the proper scheduling of charging and discharging of the BESS [35].

Modeling optimal power flow is a nonlinear problem. However, reactive power has little effect on transmitting power over long distances and therefore convex relaxation can be applied to power flow modeling to arrive at the linear direct-current optimal power flow (DC-OPF). Solving linear optimization problems is best suited for numerous linear programming techniques, such as the simplex algorithm, which can be implemented using various free and commercial solvers.

Unlike DC-OPF, BESS degradation is a nonlinear problem requiring further linearization. In this work, we linearize part of the BESS degradation approach using a multilayer perceptron (MLP) leaving the bias terms in, while using the unit activation functions of the MLP in order to preserve linearity [36].

This paper explores the methodology for sizing of BESS capacity and power rating on an interconnected bus system. Our approach takes into account the BESS degradation, the effect of outages on transmission lines, and their ampacity.

This article is organized in 6 sections. Section 4.2 describes the recent progress in BESS sizing for smart grids for transmission deferral and reliability applications. Section 4.3 describes the modelling of the system as a linear program. Section 4.4 outlines the experimental setup used in the case study, and section 4.5 discusses the results.

4.2 Related Work

Hesse et al. [37], and Martins et al. [38], size the BESS for single residential and single commercial applications using the linear programming method. They utilize the minimization of operating cost as the objective function including the feed-in tariffs and energy prices from the German power market. These studies employ the linearization of BESS calendric and cyclic aging methods proposed by Martins et al. [39]. Metwaly et al. [40] size the BESS by including it in a 24-bus IEEE reliability test system (RTS) together with a wind farm installation at multiple buses. This work takes into account the ampacity of transmission lines and simulates it using an ARMA model. It also employs a demand response method to shift the peak load to off-peak hours. A grid search approach is employed to calculate the amount of curtailed energy that needs to be removed from the system employing a particular BESS capacity. Similarly, Metwaly et al. [41] employ a grid search method for BESS sizing and the reliability of each proposed BESS size is explored on the IEEE 24-bus system. Unlike studies in [40], the work makes no use of renewable installations and uses the minimization of undelivered energy as the objective function for each time interval considered.

Hussain et al. [42] evaluate the impact of demand response intensity coupled with BESS size taking into account the uncertainties of load forecasting, intermittent generator outputs, and market metrics, by making use of their robust counterparts and modelling the problem using a robust optimization method. Vrettos et al. [43] explore the sizing of wind turbine installation, photovoltaic panel installation, and BESS in-

stallation in microgrids using the levelized energy cost as the fitness function in a genetic algorithm over the project lifetime of 20 years. Conventional generators produce a constraint enabling renewable energy source (RES) penetration of around 20%. The operating procedure of the interaction between the RES and the BESS is provided and it is demonstrated that a RES penetration of 60% is possible against the benchmark of 20%.

Mulleriyawage et al. [44] investigate the reduction in the size of BESS combined with a demand response (DR) mechanism. They show that a 63% reduction in the size of BESS for a residential home is achieved when an appropriate DR scheme is concurrently implemented. The study includes BESS degradation and and shows a 13% increase in ROI is achieved when implementing DR with BESS. The BESS size is optimized using the load consumption and available photovoltaic power, scheduling the shiftable loads, and finding the minimum energy cost for the duration of a year. The BESS is sized in [45] to support primary frequency regulation (PFR). BESS is designed to support photovoltaic solar farms. The model is evaluated using a novel performance function which counts the number of days in which BESS failed to provide adequate PFR. The optimization is performed using a linear programming method which involves a penalty function whose objective is to prevent the appearance of state-of-charge trajectories that impede the supply of an appropriate PFR. The paper shows that days in which PFR is not provided can be eliminated.

Galeela [46] performs reliability analysis on BESS degradation considering outages, transmission line aging, and DTLR, using sequential Monte-Carlo simulations. Linear programming is used to minimize the total operating cost for each time step of the simulation. This results in minimizing the expected energy not supplied. The approach is tested on IEEE 24-bus RTS and shows an improvement in the expected energy not supplied against the case without BESS. Abogaleela et al. [47] focus on using sequential Monte-Carlo simulations to reduce the amount of wind curtailment by coupling wind generation with large-scale BESS. By testing the approach on the

IEEE 24-bus RTS, they demonstrate that using 2 BESS degradation indices (EEDC and EECAD) to capture the degradation risk, a 34% reduction in wind curtailment can be achieved. Keyvani et al. [31] use mixed-integer linear programming to compute the BESS size in scenarios with high wind resource generation, available demand response scheme, and available distributed static series compensator (DSSC). The optimization is performed to minimize the capital costs of the assets to be installed. The optimization is verified on the IEEE 24-bus RTS and shows that using a combination of DTLR, BESS installations, and DSSC is a faster and cheaper alternative to upgrading the transmission lines.

This work takes into account transmission line outages, dynamic line ampacity, and BESS degradation to optimize the size of BESS for the duration of the entire considered period, using a linear programming method. This guarantees the global minimum over the entire time span. This approach can be adapted to any grid topology. It also introduces a linearization over BESS degradation relation that results in faster simulation.

4.3 System Model

The system is modelled using DC-OPF. While running the simulation, all BESSs are placed at substations and the capacity and power rating of every BESS is the same. The effect of reactive power is ignored because DTLR only affects real power [41]. The transmissible power, P, of a transmission line is calculated from the ampacity A, transmission line voltage V, and power factor p_f of the line using

$$P = \sqrt{3} V A p_\mathrm{f}, \tag{4.1}$$

where A is the ampacity of the transmission line. The objective of the simulation is to minimize the BESS capacity, E_opt, for every BESS in the system. The presence of the optimal BESS capacity then yields the possibility to optimize for the BESS

power rating, PR_{opt}. Then, for the time step t, every transmission line must satisfy

$$-R_{t,l} \leq P_{t,l} \leq R_{t,l}, \quad l \in T \tag{4.2}$$

where $R_{t,l}$ is the transmissible power of the line, and $P_{t,l}$ is the power to be sent across the line, for every transmission line l, in a set of all transmission lines T. During a line outage, the flow through the line is 0

$$P_{t \in O_l,\, l} = 0, \tag{4.3}$$

where O_l is the set of all time steps t when line l is on an outage. From DC-OPF, the power balance for each bus of the grid yields the relation

$$-L_{b,t} + G_{b,t} - PB^{\text{char}}_{b,t}/\eta_{\text{batt}} + \eta_{\text{batt}} PB^{\text{dischar}}_{b,t} + \sum_{l \in T_b} P_{l,t} = 0, \quad l \in T_b, b \in B, \tag{4.4}$$

where L is the load, G is the generation, PB^{char} is the BESS charging power, and PB^{dischar} is the BESS discharging power, all for bus b, and time step t. T_b is the set of all transmission lines feeding into bus b, and B is the set of all buses in the system. From the model presented in [37], the battery energy $E_{b,t}$ for bus b, time step t, and time interval Δt, evolves according to

$$E_{b,t+1} = E_{b,t}(1 - \frac{SD_{\text{batt}}}{d}) + (\eta_{\text{batt}} PB^{\text{char}}_{b,t} - PB^{\text{dischar}}_{b,t}/\eta_{\text{batt}})\Delta t, \tag{4.5}$$

where SD_{batt} is the BESS self-discharge constant, d is the number of time intervals in a day, and η_{batt} is the BESS efficiency. The values for SD_{batt} and η_{batt} for the specific BESS type can be found in [37]. For reliability and BESS longevity reasons, the BESS energy $E_{b,t}$ should not be less than the specified minimum percentage $SOC_{\min}$. This relation is expressed as

$$E_{b,t} \geq SOC_{\min} E_{\text{opt}}. \tag{4.6}$$

The BESS state of health (SOH), $SOH_{b,t}$, at time step t and bus b, depends on the total aging of the battery, $\text{aging}_{\text{tot } b,t}$, and is expressed as in [37]

$$SOH_{b,t} = 1 - \text{aging}_{\text{tot } b,t} \times 0.2. \tag{4.7}$$

Total aging of the BESS is a superposition of calendric aging, $\text{aging}_{\text{cal } b,t}$, which is the BESS aging due to the speeding up of the chemical reactions inside the cell, and cyclic aging, $\text{aging}_{\text{cyc } b,t}$, which is the aging of the BESS due to cycles of charging and discharging [35]. This is expressed as

$$\text{aging}_{\text{tot } b,t} = \text{aging}_{\text{cal } b,t} + \text{aging}_{\text{cyc } b,t}. \tag{4.8}$$

Using the methodology in [39], the calendric aging of the BESS for time step t, can be estimated as

$$\text{aging}_{\text{cal } b,t} = \frac{t\Delta t}{Life_{\text{cal}}^{80\%}}, \tag{4.9}$$

for all buses $b \in B$. $Life_{\text{cal}}^{80\%}$ is a constant in years, which represents the length of time that would result in the BESS degrading its state of health by 20%. Similarly, the cyclic aging of the BESS is defined recursively via the fraction of the change in the BESS energy amount to the energy of the BESS. [39] linearizes the cyclic aging process by defining it as

$$\text{aging}_{\text{cyc } b,t+1} = \text{aging}_{\text{cyc } b,t} + 0.5 \times \frac{|\Delta PB_{b,t}|}{E_{b,t}} / Life_{\text{cyc}}^{80\%}, \tag{4.10}$$

where $Life_{\text{cyc}}^{80\%}$ is defined as the number of full equivalent cycles that result in the BESS state of health degrading by 20% [37]. Both constants can be found in [37]. $\Delta PB_{b,t}$ is defined as

$$\Delta PB_{b,t} = PB_{b,t}^{\text{char}} - PB_{b,t}^{\text{dischar}}. \tag{4.11}$$

From the definition of calendric and cyclic aging in (4.9) and (4.10), it is evident that the state of health of BESS always decreases over its lifetime. The initial state of health is defined to be 1, and the initial cyclic aging is defined to be 0.

The charging and discharging BESS rates, $PB_{b,t}^{\text{char}}$ and $PB_{b,t}^{\text{dischar}}$, are limited by the optimal charging rate, PR_{opt}, and the upper and lower BESS energy. $PB_{b,t}^{\text{char}}$ is limited by the difference between the current BESS available energy, $E_{b,t}$, and the upper boundary the BESS can charge to, which is decreased by $SOH_{b,h}$ on every time

step. At the same time, the BESS cannot charge faster than the optimal power rating PR_{opt}

$$0 \leq PB_{b,t}^{\text{char}} \Delta t \leq \min(PR_{\text{opt}} \Delta t, SOC_{\max} E_{\text{opt}} SOH_{b,t} - E_{b,t}). \tag{4.12}$$

When the BESS discharges, the discharging rate $PB_{b,t}^{\text{dischar}}$ is limited by the BESS power rating PR_{opt}, and the amount of charge left in the BESS

$$0 \leq PB_{b,t}^{\text{dischar}} \Delta t \leq \min(PR_{\text{opt}} \Delta t, E_{b,t} - SOC_{\min} E_{\text{opt}}). \tag{4.13}$$

The state of health does not affect the lower boundary the BESS can discharge to, because it is a physical limitation of the BESS. It does, however, affect the upper energy level the BESS can charge to, together with $SOC_{\max}$. This limit is reduced by $SOH_{b,t}$ at every time step t

$$E_{b,t} \leq SOC_{\max} E_{\text{opt}} SOH_{b,t}. \tag{4.14}$$

The initial value of the BESS capacity, $E_{initial}$, can also be specified for time step 0 as in

$$E_{b,t=0} = E_{\text{initial}}. \tag{4.15}$$

Specifying battery capacity for time steps other than 0 can lead to infeasibility in the optimization because calendric aging predictably decreases the SOH of the BESS. The entire optimization problem then consists of (4.2-4.15) subject to minimizing E_{opt}

$$\min E_{\text{opt}}, \tag{4.16}$$

given that the optimal capacity, E_{opt}, is positive

$$E_{\text{opt}} \geq 0, \tag{4.17}$$

and the optimal power rating, PR_{opt}, is positive

$$PR_{\text{opt}} \geq 0, \tag{4.18}$$

for all t, $b \in B$, and $l \in T$.

Equations (4.10), (4.12), and (4.14) make the problem nonlinear. To linearize (4.10) a non-linear problem was solved from (4.2 - 4.18) for a small number of time steps. The term $|\Delta PB_{b,t}|/E_{b,t}$ was then computed. Various supervised learning techniques can be used to train a model to compute the ratio of $|\Delta PB_{b,t}|$ to $E_{b,t}$ in the form

$$\frac{|\Delta PB_{b,t}|}{E_{b,t}} \approx x|\Delta PB_{b,t}| + yE_{b,t} + z, \tag{4.19}$$

with x, y, z real numbers. An MLP model was trained to approximate such ratio [36]. To ensure linearity, it was required that the activation functions of every layer of the model are linear activations. The bias terms were retained in the hidden layers since they preserve the linearity of the resulting output [36]. The model was trained for 300 epochs using an Adam optimizer, mean-squared-error loss, a validation split of 30%, and a batch size of 32. The predicted linearized ratio and the actual ratio are shown in Figure 4.1. The approximation is satisfactory based on the proximity of the predicted ratios to the actual ratios and the convergence of validation loss. The approximation was shown to speed up the computation and ease the memory requirements of the computer when solving the results of the model for longer time steps. Linearizing (4.12) and (4.14) could be attempted using a similar approach. Final nonlinear programming model consists of (4.2 - 4.9), (4.11 - 4.15), (4.17 - 4.19), and an objective function in (4.16) for all t, $l \in T$, and $b \in B$.

4.4 Experimental Setup

Similarly to [41], the British Atmospheric Data Center (BADC) data from Merseyside was used, collected between 2000-2020 to obtain wind speed, wind direction, and ambient temperature [48]. Daily temperature data was averaged over multiple sensors. Wind speed and wind direction data were obtained by averaging the hourly measurements from multiple sensor readings. The data was recorded in centigrade, meters per second, and degrees for ambient temperature, wind speed, and wind direction, respectively.

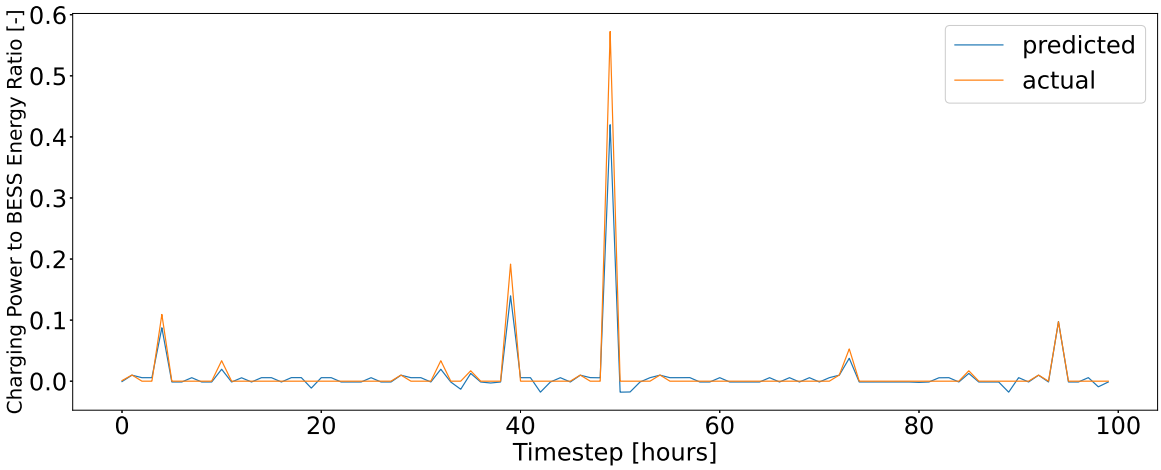

Figure 4.1: Predicted and actual change in battery energy to battery energy ratio.

For the case study, the simulation was performed on the IEEE 24-bus RTS [49]. It is a test grid, consisting of 24 buses. Some of the buses have loads and generators on them. The BESSs were placed at each bus with the load. The effects of synchronous condensers, transformers, and inductors were ignored. Transformer outages were not taken into account to focus only on the transmission line outages.

The simulation was discretized into hourly intervals, resulting in the number of time intervals in a day, $d = 24$. The simulation was ran for a period of 672 hours (1 month). The loads and generator capabilities for every hour are described in [49]. Ambient temperature has the weakest effect on the ampacity values and, similar to [41], the ambient temperature was chosen as the highest ambient temperature for the season. The values for solar irradiance, conductor temperature, horizontal angle, and elevation were taken to be conservative. Similar to [41], the 138 kV side of the RTS was taken to be the Drake ACSR, and the 230 kV side of the RTS was taken to be the Lapwing ACSR.

The BESS in the analysis is lithium-nickel-manganese-cobalt (NMC) in composition. For BESS degradation calculations, the values found in [37] were used. Similarly to [41], the size of all generators and all loads was increased by 4 to stress the system. The calculations of the ampacity were then performed using the IEEE-738

standard [50]. For outage information on the transmission lines, the permanent and transient outage rates were found in [49]. No relaxation was used in the feasibility tolerance of the solver, other than its default tolerance [51]. The maximum discharging of the BESS was taken to be no more than 20% of the optimal capacity and the maximum charging was taken to be no more than 80% of its optimal capacity. The initial energy capacity of every BESS at the start of the simulation interval was set to equal 80% of the optimal BESS capacity.

4.5 Discussion

The linear programming task was solved using the Gurobi commercial solver using the nonconvex parameter setting. Running the simulation for 672 hours shows that the SOH of any bus did not degrade by more than 0.156% and degraded by at least 0.148%. The SOH of selected buses are shown in Figure 4.2. Using the BESS at bus 18 as an example, its charging behavior can be observed in Figure 4.3. The figure shows that the BESS at bus 18 charges and discharges significantly more often before 110 hours than after. SOH curves resemble linear trends. The linear downtrend for BESS at bus 18 accelerates with increasing charging and discharging BESS action before 110 hours of operation, increasing the impact cyclic aging has on the SOH of the BESS, as shown in Figure 4.2. High levels of charging and discharging of a BESS have the potential to decrease SOH and shorten its service life.

Without the load multiplier, the total generating capacity of the system is 3405 MW against the total load of 2850 MW. DTLR of transmission lines places a limitation on how much power can be transferred between buses. Since buses 3, 5, 6, 8, 9, and 10 on the 138 kV side, and buses 14, 19, and 20 on the 230 kV side of the RTS have a load on them, but do not have generators, the power to satisfy the load at those buses has to come partially from the BESS located at those buses, forcing the need in the system for non-zero BESS capacity. The optimal BESS capacity was calculated to be 217 MWh with 217 MW power rating. The power rating was not optimized but due

to choice of the time interval cannot be higher than capacity in this simulation. If the load multiplier of 4 is replaced with 3, no BESS storage is necessary. This means that the transmission system is over-designed and the ampacity of the transmission lines does not affect the ability of power to flow between buses. The performed simulation ran in 15 minutes on a 32 GB RAM, AMD Rizen 5, 3.4 GHz.

4.6 Conclusion

We have presented here general methodology for sizing BESS capacity and power rating that takes into account battery degradation, transmission line outages, dynamic line rating, and load growth. The method can be based on non-linear programming or the grid search approach. The method was tested on 2-bus grid setup in Canada. We also presented a BESS capacity sizing evaluation method based on grid search simulations. Future work can include applying a probabilistic approach to sizing and using more accurate BESS degradation methodology. This work can also be extended to calculate the optimal size of each individual BESS at every bus.

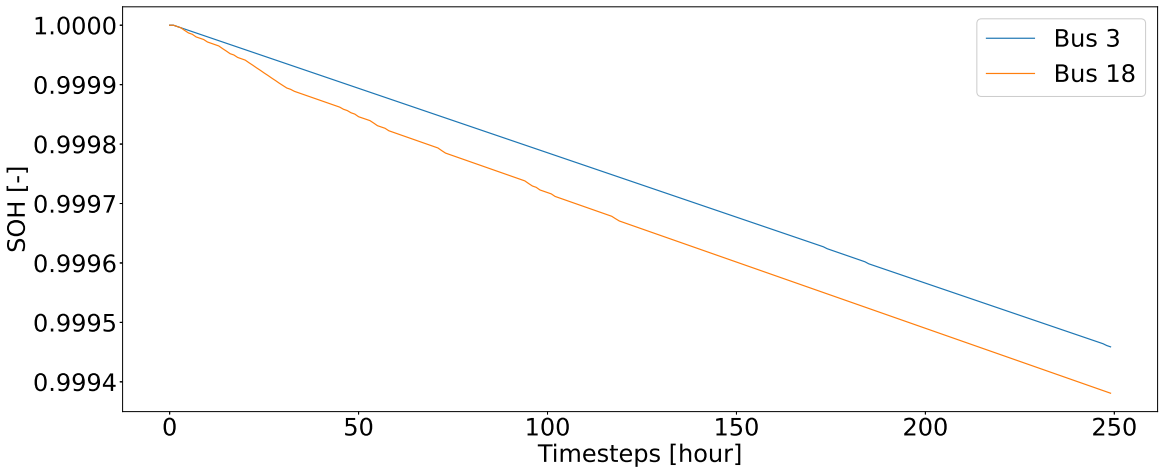

Figure 4.2: SOH of BESS at buses 3, 18.

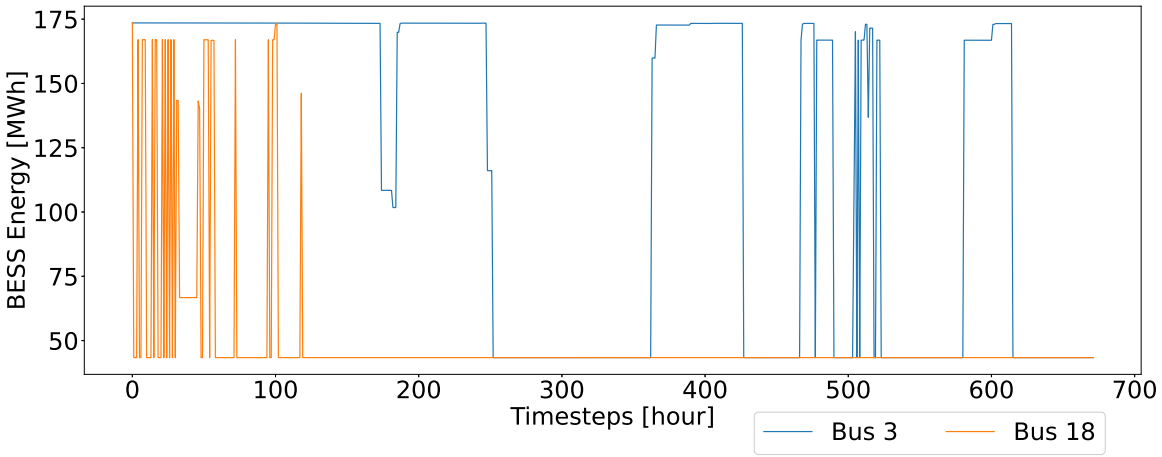

Figure 4.3: Energy of BESS at buses 3, 18.

Chapter 5

Deep Learning BESS Control

5.1 Introduction

The introduction of battery energy storage system (BESS) units into utility-scale transmission grids has the potential to enable large-scale renewable energy integration by storing energy when it is available and discharging when more energy is required [52]. When an accurate load forecast is known, it can be combined with generator power limits and grid topology to calculate the most appropriate outputs for the generators, typically implemented using linear programming (LP) methods [53]. Determining an accurate load forecast and the forecast horizon are then crucial for effective dispatches on the grid. Forecasting has benefited from recent applications of artificial neural networks (ANNs), including long-short term memory networks (LSTMs), convolutional neural networks (CNNs) as well as their combinations [54].

Overhead lines (OHL) are designed to operate below a maximum temperature. Line temperature varies with ambient temperature, wind speed, wind direction, solar irradiance, precipitation, and operating current. Wind speed and temperature have the highest impact on the maximum temperature of the conductor [33], which can be used to calculate the maximum current in Amperes the OHL can carry. This current is referred to as dynamic thermal line rating (DTLR). For reliability and planning purposes the rating of the OHL is kept constant and is referred to as static line rating (SLR). Using DTLR instead of SLR in real-time operations and planning can alleviate

congestion, and defer the construction of new lines [32]. Forecasting DTLR can then be used in conjunction with forecasted load to improve the performance of power system operations [55].

This work proposes a step-ahead battery action forecasting method based on bidirectional attention-based CNN-LSTM architectures that takes into account dynamic line rating, transmission line outages, and BESS degradation. The method also makes use of the sliding window approach to determine the forecasting horizon. The method is tested on 24-bus reliability test system [49] utilizing British Atmospheric Data Center (BADC) Merseyside weather dataset [48], using hourly data.

This article is organized as follows. Section 5.2 discusses recent progress in applications of load forecasting methods in optimal BESS operating strategies. Section 5.3 describes the BESS sizing and load forecasting. Section 5.4 discusses the determination of the forecast horizon and battery action forecasting. Section 5.5 presents the results.

5.2 Related Work

Vrettos et al. [43] propose a method to determine component sizes of photovoltaic panels (PVs), wind turbines, and BESS utilizing a genetic algorithm which includes a 30-min load forecast as an input. The load is forecasted using a persistence model. The fitness function is based on a linear combination of levelized energy cost and Renewable Energy Sources (RES) penetration level. Testing the system on a microgrid in Greece allowed for 60% penetration of RES. Reihani et al. [56] use polynomial regression to forecast load for the following day. The BESS is effectively applied in a peak shaving, and separately, in a voltage regulation task, and is shown to smoothen the load. Zheng et al. sample uncertainties in wind forecasting, load forecasting, and solar energy forecasting from a Gaussian distribution for day-ahead forecast, and optimizations using Natural Aggregation Algorithm, Differential Evolution, and Particle Swarm optimization algorithms were compared. The method was shown to decrease

energy cost for industrial partner [57]. Chapaloglou et al. in [58] apply a feed-forward neural network (FFNN) for day-ahead load forecasting. The FFNN used the previous day's load as well as information about the day of the week to make a forecast. The forecasted load was used in conjunction with diesel and PV generators to shave peaks on an island microgrid when the nightly peak occurred. The system was modelled using optimal power flow. The forecasted values were fed as input into a Hierarchical Agglomerative Clustering algorithm to determine whether a nightly peak is likely to occur. The method was shown to reduce the capacity and enable smoother operation of diesel generators, reduce the peak, and offer the potential of higher penetration of RES integration. Faraji et al. [53] propose a 2-level optimization model for the optimal utilization of BESS and RES. In the first level, 30-day historical load data is used to make a day-ahead forecast. ANNs are used to forecast the load data. Mixed-integer LP is used for the BESS action optimization. If the measured load differs from the forecasted load outside a certain threshold, a 2nd level corrective action using an ANN is applied. The method has been shown to reduce the prosumer operation cost by 7%.

Alhussein et al. use CNN-LSTM model for short-term residential load forecasting. Xiong et al. [59] uses encoder-decoder architecture with bidirectional LSTM blocks to forecast short-term load. The importance of the input features is evaluated using an attention mask which is then served as an input to the bidirectional LSTM layer to be sent to the decoder. Similarly, Sehovac et al. [60] use encoder-decoder architectures with attention blocks for load forecasting. They test the effectiveness of the types of recurrent neural network units and found Bahdanau attention outperforms other models. Lin et al. in [61] propose an LSTM model with attention for the probabilistic load forecast. In the first stage, the encoder model uses attention to find most important input features while in the 2nd stage, the attention mechanism is used in the decoder to find time dependencies. Probabilistic forecast is then obtained using a pinball loss function.

We consider the performance of attention-based bidirectional LSTM-CNN neural network architectures for load and ampacity forecasting considering line outages, DTLR, and BESS degradation. Discussion of efficient selection of forecasting horizon is also presented.

5.3 System Model

Load balancing relations being linear make LP methods a natural candidate for battery capacity sizing [42]. Due to non-linearity in BESS degradation, a non-linear programming (NLP) method is used with an objective function of minimizing BESS operation. Once the forecasted load and forecasted DTLR are known, they can be used as inputs into the BESS operation method to output appropriate BESS charging and discharging actions. A graphical depiction of the BESS action prediction process is shown in Fig. 5.1.

5.3.1 BESS Sizing Methodology

The description of the methodology for BESS capacity sizing is given in Section 4.3.

5.3.2 Load and Ampacity Forecasting

LSTM networks are recurrent neural networks that were created to alleviate the problem of vanishing gradient by allowing the gradient to access the forget gate's activations. Bidirectional LSTMs (BiLSTM) are combinations of two concurrent LSTM layers with layers typically added or concatenated. One of the LSTM layers is computed forward and the other one backward [62]. Sequence-to-sequence (seq2seq) models were introduced in the natural language processing domain but have found applications in time-series processing [63]. One of the implementations of seq2seq is encoder-decoder [64] which involves encoding a context vector as a representation of the input features and decoding it using the decoder network. Recent successes with a combination of seq2seq, LSTM, CNN, bidirectionl RNN, and attention-based

models inspire an approach that utilizes those architectures [59, 65].

The CNN-LSTM model consists of 2 concurrent 1-dimensional convolutional layers with 64 filters, kernel size of 3, and ReLU activations. This is followed by a 1-dimensional max-pooling layer with a pooling size of 2, which down-samples, and is followed by a flattening layer. A repeat vector layer copies the output to match the size of the output dimension [28]. This is followed by an LSTM layer with 200 units, ReLU activation, and returning the hidden values for each timestep of the input sequences. Repeat vector enables the network to produce the output dimension number heads that are put through the LSTM layer. A fully-connected layer with 100 units and ReLU activation is wrapped in a TimeDistributed layer [28], which allows for processing each fully connected layer output one-by-one. The output is put through another fully connected layer with a single unit which is also processed with a TimeDistributed wrapper.

A CNN-BiLSTM model is a variation on the above model, with the first LSTM layer containing 200 cells processed with a Bidirectional wrapper, which implements the bidirectional functionality. Attention mechanism was introduced in [66] to keep information propagated with longer sequences. For a time-series $\boldsymbol{y}$, the output of an LSTM layer being $\boldsymbol{h}_t$ at a time step t, and the output of the LSTM layer propagated backward being $\overline{\boldsymbol{h}}_s$, the attention score, $\boldsymbol{s}_t$, is computed as:

$$\boldsymbol{s}_t(\boldsymbol{h}_t, \overline{\boldsymbol{h}}_s) = \boldsymbol{h}_t \cdot \overline{\boldsymbol{h}}_s, \tag{5.1}$$

at time step t. The attention scores, $\boldsymbol{s}_t$, are then normalized with a softmax function

$$\alpha_{t,i} = \frac{e^{s_{t,i}}}{\sum_j e^{s_{t,j}}}, \tag{5.2}$$

to compute the weights, which are used to compute the weighted value via:

$$\boldsymbol{c}_t = \sum_s \alpha_{t,s} \overline{\boldsymbol{h}}_s. \tag{5.3}$$

$\boldsymbol{c}_t$ is then used in later layers in the neural network. We inserted this attention computation after the first bidirectional LSTM layer and prior to the TimeDistributed

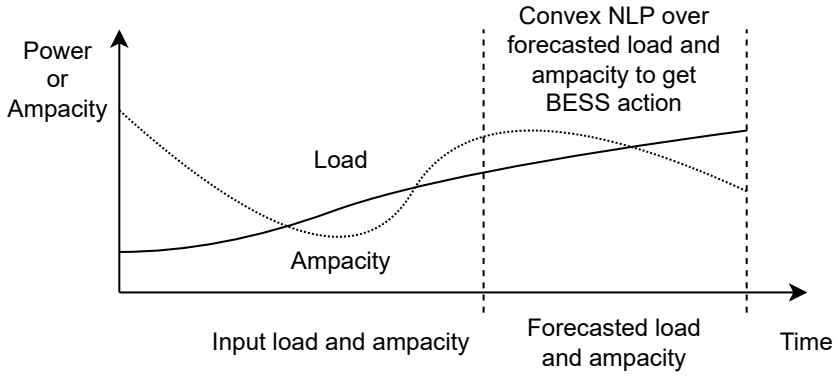

Figure 5.1: Forecasting BESS action with forecasted load and ampacity

wrapper and call this model CNN-BiLSTM-1Atn. In a CNN-BiLSTM-2Atn model the output of the first attention layer is used together with the output of backward-propagated LSTM in another attention layer.

Seq2seq model tested here consisted of 2 concurrent LSTM layers in the encoder followed by two concurrent LSTM layers in the decoder with 75 cells in each layer. The encoder output is repeated the output dimension number of times and the output of the decoder is processed with a fully connected layer with a single unit in a TimeDistributed wrapper.

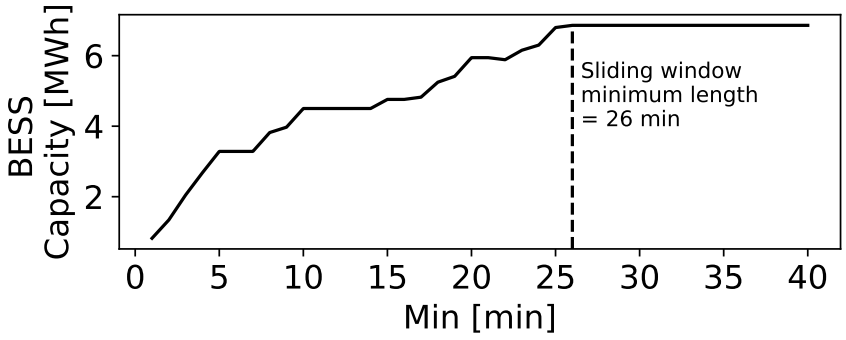

Figure 5.2: Sliding window chart for 2-bus system

5.4 BESS Control

5.4.1 Sliding Window

The length of the forecast horizon has to capture every scenario that may occur over the distribution of data on the 24-bus RTS. Provided the BESS starts out at 80% of its maximum capacity at the beginning of the simulation, a sliding window can be applied over the length of the data. First, 1-hour sliding window is chosen, and is then moved forward a single time-step. For each of the sliding windows a BESS capacity is calculated and stored. The highest capacity from the stored list is then chosen. Then the sliding window is increased to 2 hours and the process is repeated until the length of the sliding window is the same as the length of the data. A curve can then be constructed showing the sliding window length against the maximum BESS capacity required for that sliding window.

The start of the plateau of the curve indicates the smallest sliding window size that takes into account all possible cases over the distribution of data. An example of such a curve is shown in Fig. 5.2 for a BESS modelled in a 2-bus grid. However, it is unreasonable to expect that a BESS can be fully charged at the start of each time interval, and in some cases the BESS will be fully discharged with the energy needed to be delivered. Such situations can make the NLP infeasible.

To ensure feasibility, the capacity of the BESS calculated needs to be increased by the difference between $SOC_{\max}$ and $SOC_{\min}$. Doing so will enable the BESS to supply enough energy even if it was discharged. For the 24-bus RTS we assume the forecast horizon of 12 hours with 48 hours as the input into the forecasting model, however, the minimum sliding window size may be computationally expensive to get.

5.4.2 BESS Action Forecasting

Initially, the BESS capacity and power rating need to be obtained. SOH, cyclic aging, and line outage statuses are initialized. Battery capacity and power rating

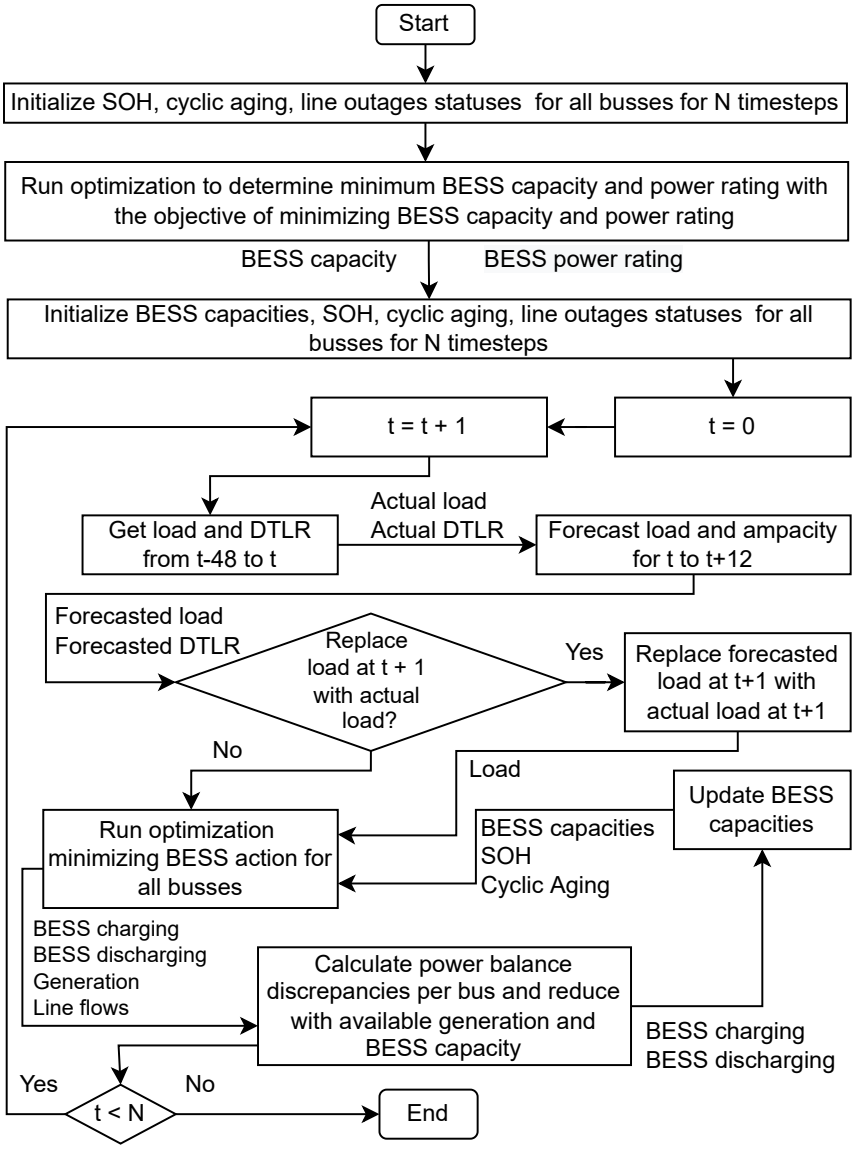

Figure 5.3: Process for calculating BESS action

are calculated for N simulation steps based on optimization process summarized in equations (4.4)-(4.16) with the objective function expressed in equation (4.16). For time step t, in the time units of the application of choice, the BESS capacities, states of health, and cyclic aging are initialized. The service/out-of-service status of the transmission lines are also initialized based on the outage rate of every line for the simulation length N. Calendric aging is deterministic and can be calculated for each BESS based on the time step of the simulation.

The load and ampacities for time steps $t-48$ to t for each bus are obtained. These loads and ampacities are then fed into the forecasting model to obtain load and ampacity forecast values for every bus for time steps t to $t+12$.

At this point the forecasted load can be used in the convex NLP optimization, or the forecasted load at time step $t+1$ can be replaced by the actual load at $t+1$. The optimization then runs with the objective function of minimizing the sum of BESS charging and discharging power for every bus, expressed as

$$\min \sum_{b} \sum_{t<N} (|PB_{b,t}^{\text{char}}| + |PB_{b,t}^{\text{dischar}}|), \quad b \in B. \tag{5.4}$$

The BESS charging, BESS discharging, generator output, and line flows are extracted as the outcome of the simulation.

Then the BESS charging, BESS discharging, generation, and power flows are inserted in equation 4.4 and the power balance discrepancy is calculated at every bus, with any discrepancies recorded. The BESS charging and discharging actions are used to update the capacities, and cyclic aging for each bus, based on equations 4.5 and 4.10, respectively.

Unless the simulation length N is exceeded, the time step t is increased and the process repeats again, with new BESS capacities and aging values. The process is shown in Fig. 5.3.

5.5 Discussion and Conclusion

The ambient temperature was chosen as the highest in each of the 4 seasons. The load and generator data were increased 4 times to ensure system is at its limits [41]. Drake and Lapwing conductors were chosen for the 138kV and 230kV lines, respectively. DTLR values are calculated from IEEE-738 standard. Batteries were placed at each bus with the load and each BESS discharged no less than and charged no more than 20% and 80% of the BESS capacity. Lithium-nickel-manganese-cobalt BESS was assumed to be used with constants found in [37].

Table 5.1: Model Performance on Bus 1 Load Dataset

	MAPE (%)			**MSE** ($10^6 \cdot \text{MW}^2$)		
Model	***min***	***max***	***mean***	***min***	***max***	***mean***
seq2seq	0.6	16.1	3.2	4.2e-6	3.1e-3	1.6e-4
CNN-LSTM	0.8	14.7	3.9	5.3e-6	2.6e-3	1.9e-4
CNN-BiLSTM	0.4	24.8	2.6	2.4e-6	5.7e-3	1.4e-4
CNN-BiLSTM-1Atn	0.4	21.9	2.7	2.1e-6	5.1e-3	1.6e-4
CNN-BiLSTM-2Atn	0.5	18.1	3.4	3.5e-6	3.1e-3	1.6e-4

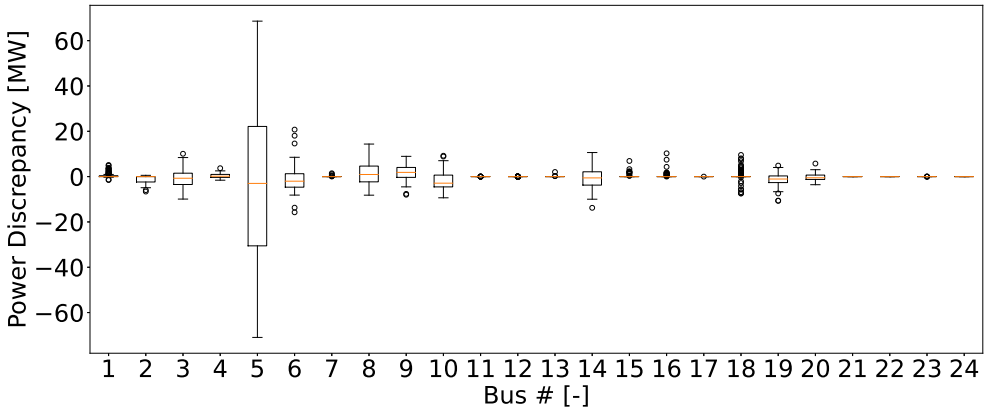

Figure 5.4: Bus discrepancies with forecasted load at $t + 1$.

Applying these models to the bus loads we find the CNN-BiLSTM model for bus 1 outperformed based on mean and minimum absolute percentage error (MAPE) and mean squared error (MSE), as shown in Table 5.1. The error is calculated for each testing sample and maximum, minimum, and mean value of the error are shown. To improve model training load and ampacity values were scaled down by a factor of 1000 and 10000, respectively. Models for load forecasting and Lapwing ampacity were selected similarly, with CNN-BiLSTM-Atn1 and CNN-BiLSTM-Atn2 models outperforming others for Drake and Lapwing conductors, respectively.

Sizing the BESS for simulation duration of 672 hours (4 weeks) resulted in BESS

capacity of 217 MWh and power rating of 217 MW. Increasing the capacity by 60% as explained in section 5.4.1 and choosing to replace the load with actual load at time step $t + 1$ resulted in the bus discrepancies that were practically 0. Choosing not to replace the load at $t + 1$ with actual load, the maximum discrepancy is observed on bus 5 at -71 MW, as shown in Fig 5.4. For other busses the discrepancies are less than 20 MWs. The discrepancies are due to forecasting errors and forecast horizon not necessarily being as long as needed. Forecasting strategy distributes load from other buses onto bus 5. More accurate load forecast would reduce the bus discrepancies.

This work presents a BESS operation method that includes forecasted load and ampacity calculated with CNN-LSTM architecture variations, and then uses those forecasted quantities inside linear program to predict a step-ahead BESS action. As future work, an improvement to the forecasting methods and adding RES to 24-bus RTS can be made.

Chapter 6

Deep Reinforcement Learning BESS Control

6.1 Introduction

Incorporating a battery energy storage system (BESS) into a utility-scale transmission system can increase its reliability, its control can be challenging due to the uncertainty in forecasting operational parameters [67]. Deep Reinforcement Learning (DRL) is a framework combining neural networks with reinforcement learning function approximators to find behavioral policies that approximate actions in complex environments given [68]. DRL methods have been shown to be effective at solving problems in demand response [69], voltage regulation [70], transactive energy markets [71], and are being incorporated into smart grids at an accelerating pace.

Deep deterministic policy gradient (DDPG) [72], multi-agent DDPG (MADDPG) [73], soft actor critic (SAC) [74], and multi-agent SAC (MASAC) [75] methods are methods that have been found to be successful at tasks of BESS demand response [75] and voltage control [76]. These algorithms are suitable for applications where state and action space are continuous, and may be effective at solving non-linear BESS control problems involving continuous action and state space.

Transmission lines are designed and rated at maximum conductor temperatures that is representative of worst-case scenarios and assumed to be static or varied only seasonally. In reality, line temperatures vary with ambient temperature, solar irradi-

ance, precipitation and notably wind speed and direction, [33]. Compared to static line rating (SLR), dynamic thermal line rating (DTLR) takes the real-life temperature changes into account to estimate the maximum ampacity, or the highest current the line can carry at the actual operating conditions. DTLR can be multiple times higher than SLR [32]. Using DTLR instead of SLR in planning and operation of transmission lines could relieve network congestion and reduce or delay the need for new construction. Recent advancements in deep learning enable more accurate DTLR and load forecasts that can be used in combination with outage schedules to better allocate resources and plan for the future [77].

System demand does not necessarily coincide with the most favorable environmental conditions, which limits the practical effectiveness of DTLR on its own. Adding a BESS can help to buffer loads to when DTLR can be effectively taken advantage of, if it can be adequately controlled.

Mixed-integer Linear Programming (MILP) is often used for sizing BESS capacity in a multi-bus utility network given the topology of the grid and generator capacities. Once the BESS is sized given costs and load data, the prediction of charging and discharging, generator output, and power flows across the lines can be calculated using a combination of forecasting and MILP methods [42].

This paper considers how the integration of a BESS can be used to optimize use of DTLR by increasing power capacity and improving the reliability of the system. However, it also adds new operational challenges to maximize the benefits offered by DTLR. This study develops, and evaluates a DRL-based controller for a practical case considering transmission line outages and storage system degradation using a modified IEEE 6-bus reliability test system (RTS) [78] is used. The controller is designed using several common DRL methods and then augmented by a 1-step load and transmissible power forecaster. Hourly data from the British Atmospheric Data Center (BADC) Merseyside weather dataset [48] is used. Prior to the application of DRL algorithms, the non-linear programming (NLP) method is used to size the BESS

appropriately.

Section 6.2 covers the background, including BESS sizing (6.2.1), deep reinforcement learning algorithms (6.2.2), and forecasting of load and transmissible power (6.2.3), and other recent applications of reinforcement learning algorithms in the power system (6.2.4). The optimization problem is formulated in Section 6.3 and experimental setup described in Section 6.4. Obtained results are presented and discussed in Section 6.5. Finally, Section 6.6 provides major conclusions and possible directions of future work.

6.2 Background and Related Work

6.2.1 BESS Capacity Sizing

The BESS capacity sizing methodology is presented in Section 4.3. As a reminder, the balance of power at each bus b must be satisfied as in:

$$-L_{b,t} + G_{b,t} - PB_{b,t}^{\text{char}}/\eta_{\text{batt}} + \eta_{\text{batt}} PB_{b,t}^{\text{dischar}} + \sum_{l \in T_b} P_{l,t} = 0, \quad l \in T_b, b \in B. \tag{6.1}$$

The BESS charging power is bounded by the power rating, and the maximum amount the BESS can charge to, expressed as [37]:

$$0 \leq PB_{b,t}^{\text{char}} \Delta t \leq \min(PR_{\text{opt}} \Delta t, SOC_{\max} E_{\text{opt}} SOH_{b,t} - E_{b,t}). \tag{6.2}$$

The discharging power of the BESS is bounded by the power rating, and the amount of power the BESS can discharge:

$$0 \leq PB_{b,t}^{\text{dischar}} \Delta t \leq \min(PR_{\text{opt}} \Delta t, E_{b,t} - SOC_{\min} E_{\text{opt}}). \tag{6.3}$$

6.2.2 Deep Reinforcement Learning

DDPG and MADDPG

DDPG is a model-free off-policy actor-critic method involving target actor and target critic networks which are used to compute the critic loss. This algorithm is well suited

for continuous state and action spaces [72]. DDPG uses a replay buffer to store past transitions and uses them to train the actor and critic networks. Given that s is the state, a is the action, and r is the reward, the tuple (s_i, a_i, r_i, s_{i+1}) is then the batch from the replay buffer W. The target network weights $\theta^{Q'}$ are updated via a soft update [72]:

$$\theta^{Q'} = \tau\theta^{Q} + (1-\tau)\theta^{Q'} \tag{6.4}$$

where $Q(s, a|\theta^{Q})$ and $Q'(s, a|\theta^{Q'})$ are the critic and target critic networks, respectively, and τ is the polyak constant. $\mu(s|\theta^{Q})$ is the actor network and $\mu'(s|\theta^{Q'})$ is the target actor. The critic loss L_{critic} is computed as [72]:

$$L_{critic} = \frac{1}{N_s}\sum (y_i - Q(s_i, a_i|\theta^{Q}))^2 \tag{6.5}$$

where $y_i = r_i + \gamma Q'(s_{i+1}, \mu'(s_{i+1}|\theta^{\mu'})|\theta^{Q'})$, and N_s is the batch size. The actor loss is updated via:

$$\nabla_{\theta^{\mu}} J \approx \frac{1}{N_s}\sum \nabla_a Q(s_i, \mu(s_i)|\theta^{Q})\nabla_{\theta^{\mu}}\mu(s_i|\theta^{\mu}) \tag{6.6}$$

Exploration in DDPG is ensured by adding Gaussian noise to the actions [72]:

$$\mu'(s_t) = \mu(s_t|\theta^{\mu}) + \epsilon, \tag{6.7}$$

where μ' is the exploration policy, and $\epsilon \sim \mathcal{N}(1, 0)$. Once the noise is added the actions are clipped to the required ranges. When DDPG is used in an inference task the noise is not added to the actions.

MADDPG extends DDPG into the multi-agent domain via the centralized training, decentralized execution approach where each agent outputs actions per its own actor network but actions and observations from all agents are concatenated together to be passed as inputs into each agent's critic network [73]. Similarly to DDPG, exploration is ensured by adding noise to the actions, and target networks are updated with the soft update. The actor loss is then updated [73]:

$$\nabla_{\theta_i} J \approx \frac{1}{N_s}\sum \nabla_{\theta^i}\mu_i(o_i^j)\nabla_{a_i} Q_i^{\mu}(s^j, a_1^j, ..., a_{N_{\text{agents}}}^j), \tag{6.8}$$

for each agent j, where s^j is the global state, $a_i^j = \mu_i(o_i^j)$, o^j is the agent j's observation, and N_{agents} is the number of agents. Each agent receives it's own reward r^j.

SAC and MASAC

SAC is an off-policy actor-critic algorithm that uses an entropy regularization coefficient α for exploration. Similarly to Twin-delyaed DDPG (TD3) [79], SAC trains two critic policies and picks the minimum one [74]. Entropy regularization trains a policy in a stochastic way, and exploration is done on-policy. The policy network is updated via [74]:

$$\nabla_\theta \frac{1}{N_s} \sum (\min_{i=1,2} Q_{\theta_i^Q}(s, \widetilde{a}_\theta(s)) - \alpha \log \mu_\theta(\widetilde{a}_\theta(s)|s)) \tag{6.9}$$

where $\widetilde{a}_\theta(s) \sim \mu_\theta(\cdot|s)$. Soft update is used to correct the weights of the target networks, similarly to DDPG. Centralized training, decentralized execution is used to generalize SAC to MASAC, as in MADDPG.

PINNs

Physics-informed neural networks [80] (PINNs) are neural networks with the physical laws governing the problem incorporated into the loss function or the neural network architecture. In some cases, PINNs require fewer data and less complicated neural network architectures. From equation (6.1) we can observe that the sum of the actions representing the generator power, BESS charge or discharge power, and line flow from the policy network must add up to 0 for all busses in the network, represented as $|\sum_j \widetilde{a}_\theta^j(s)|$, where j refers to the individual generator, BESS, and line flow actions. Using SAC as the algorithm, this physical knowledge can be incorporated into the policy loss network as:

$$\nabla_\theta \frac{1}{N_s} \sum (\min_{i=1,2} Q_{\theta_i^Q}(s, \widetilde{a}_\theta(s)) - \alpha \log \mu_\theta(\widetilde{a}_\theta(s)|s) + \xi|\sum_j \widetilde{a}_\theta^j(s)|), \tag{6.10}$$

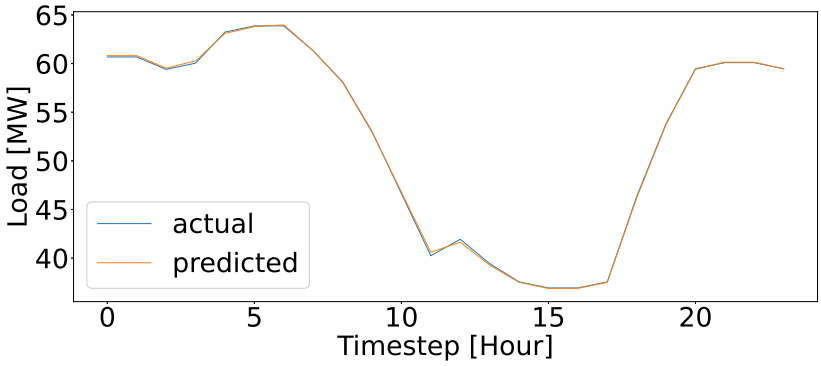

Figure 6.1: Predicted and actual load for bus 4.

where ξ is a small regularization constant. Backpropagation may be forced to minimize the introduced $\xi|\sum_j \widetilde{\alpha}_\theta^j(s)|$ term, which may improve the learning process of the algorithm and improve its convergence.

6.2.3 Load and Ampacity Forecasting

Combining convolutional neural networks with bidirectional long-short term memory networks (CNN-BiLSTM) has been shown to be effective at forecasting load [65]. The CNN-BiLSTM model with a non-trainable attention layer is used to forecast the load and transmissible power forward. Two one-dimensional convolutional layers, with 64 kernels, 3 kernel size, and ReLU activation are used in sequence, followed by a one-dimensional max-pooling layer with a pooling size of 2. Afterwards, the output is flattened, repeated once, and put through a BiLSTM layer. Two separate LSTM layers, with 200 units and ReLU activation, act on the output and are put through a non-trainable attention layer. Its output goes through another attention layer with the output of the 2nd LSTM layer. This is put through 2 consecutive TimeDistributed wrappers, the first with 100 units and the 2nd with a single unit. The forecasted and predicted loads on bus 4 are shown in Figure 6.1.

6.2.4 Related Work

Zhang et al. [69] applied SAC, DDPG, Double Deep Q-Network (DDQN), and Particle Swarm Optimization (PSO) algorithms to the problem of controlling a combined heating power plant (CHP), wind turbine generator (WTG), BESS output, and wind power conversion ratio in a network heating natural-gas power network. SAC outperformed other algorithms. When training on Danish load data, 24-step episodes of 1-hour each were considered. To account for the proper reward function, constraint violations were assigned a penalty amount and the SAC algorithm learned to virtually eliminate over-constraint violations. The problem was tested on 3 scenarios and operating system cost minimization was taken as the reward.

Khalid et al. in [70] applied TD3, DDPG, Genetic Algorithm (GA), and PSO to the problem of frequency control in a two-area interconnected power system. The algorithms output the values of the proportional, integral, and derivative gains of the PID controller. A linear combination of the absolute values of the frequency deviations and tie-line power was used as the reward. The purpose of the simulation was to reduce the Area Control Error between the two interconnected areas. TD3 outperformed the other algorithms and was able to maintain the frequency of the system within $\pm$ 0.05 Hz over 60 seconds of operation. Yan et al. in [81] employed DDPG to minimize the sum of the generation, battery aging, and unscheduled interchange costs, taking into account BESS degradation. Over 200 seconds DDPG was shown to be effective at keeping the frequency deviation within $\pm$ 0.05 Hz limits. The critic neural network was trained separately before applying DDPG. Then the actor network was trained using the pre-trained critic network.

Zhang et al. in [82] tested TD3, SAC, DDPG, DQN, Advantage Actor Critic (A3C), Cycle Charging (CC), and Proximal Policy Optimization algorithms on the task of managing a microgrid using Indonesian data. The algorithms were tested with the reward function based on the linear combination of the negative of the

fuel consumption over the year and the total number of blackouts occurring. The microgrid was assumed to contain BESS, photovoltaic (PV) panels, a wind turbine, a diesel generator, and customer loads. TD3 outperformed other algorithms, with DQN being the close second. Cao et al. in [76] use MADDPG to control voltage drop in IEEE 123-bus RTS. They assign a reward function as the sum of the absolute voltage deviations per bus and demonstrate effective control.

Cao et al. in [75] applied MASAC algorithm, multi-agent TD3 (MATD3), and decentralized and centralized training versions of SAC algorithm, to the task of voltage control on the IEEE 123 bus system. The control region was divided into 4 sub-regions and multiple agents were assigned to control the static VAR compensator and PV output. The reward function consisted of the linear combination of voltage deviation, penalty terms, and curtailment. Centrally-trained SAC outperformed other algorithms, with MATD3 performing similarly. Over 90 seconds, both algorithms were able to regulate the voltage to be within $\pm$ 0.05 p.u. Hussain et al. in [67] trained the SAC algorithm to effectively control the BESS at a fast-charging EV station. SAC was compared with TD3 and DDPG and outperformed the other algorithms. The reward function was composed of the load reward, the battery discharging and charging reward, and the peak load reward. A summary of recent studies using RL for BESS control is shown in Table 6.1.

6.3 Problem Formulation

The experiments were conducted using a modified 6-bus IEEE test grid shown in Figure 6.2. This system is selected as the test bed for the experiments to demonstrate the application of RL algorithms on a relatively simple setup while preserving the properties of variable load and allowing the presence of numerous buses and multiple BESSs. As shown in the diagram, BESSs and loads are present at busses 4, 5, and 6, together with 11 transmission lines, comprising 17 actions. It is expected that, for systems with higher numbers of buses, training and convergence will require a higher

number of episodes but the behavior of the system will be qualitatively similar.

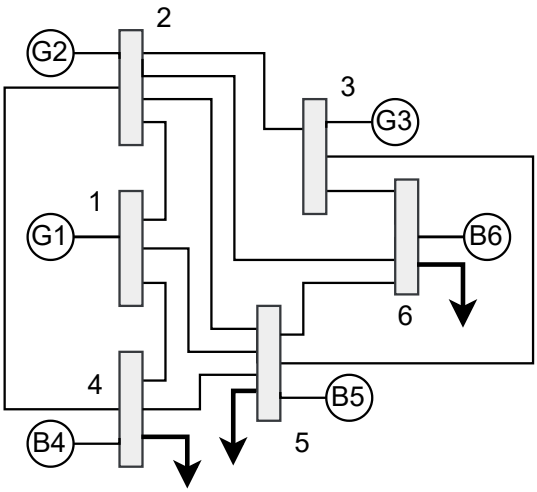

Figure 6.2: Modified IEEE 6-bus test grid.

6.3.1 Single-agent Setting

With DDPG, in a single-agent setting, a single actor network $\mu_{DDPG}(s(t))$ will output all 17 actions. The generator action is derived from an actor node with a sigmoid activation and is then multiplied by the value of the maximum action of the respective generator. This is expressed as:

$$G_{b,t}^{\text{clipped}} = \text{clip}(a_{GEN,b,t} G_{b,\max} + \epsilon,\ 0,\ G_{b,\max}), \tag{6.11}$$

where $G_{b,t}^{\text{clipped}}$ is the clipped generator action, $a_{GEN,b,t}$ is the output of the actor network for generator action at bus b, $G_{b,\max}$ is the maximum generation at bus b, and $\epsilon \sim \mathcal{N}(1, 0)$ is the Gaussian noise. For the power flow across each transmission line, the value is derived from the node with tanh activation and is then multiplied by the value of the maximum transmissible power in all time steps t, to ensure that power across lines can flow backwards, before being clipped between the negative and positive values of the transmissible power at time t. This can be written as:

$$P_{l,t}^{\text{clipped}} = \text{clip}(a_{LINE,l,t} R_{l,\max} + \epsilon,\ -R_{l,t},\ R_{l,t}), \tag{6.12}$$

where $P_{l,t}^{\text{clipped}}$ is the clipped line action, $a_{LINE,l,t}$ is the output of the actor network for the line action, and $R_{l,\max}$ is the maximum absolute line rating for line l for all time steps t in set H. For each BESS, the value is derived from the node with tanh activation and is then multiplied by the power rating of the BESS, before being clipped by the positive amount the BESS can charge at the time step t, and negative amount the BESS can discharge at time step t. The clipping values for the BESS action are calculated using equations (6.2) and (6.3). This can be expressed as:

$$\begin{aligned} PB_{b,t}^{\text{clipped}} = \text{clip}(&a_{BESS,b,t} PR_{opt} \Delta t + \epsilon, \\ &E_{b,t} - SOC_{\min} E_{opt}, \\ &SOC_{\max} SOH_{b,t} E_{opt} - E_{b,t})/\Delta t, \end{aligned} \tag{6.13}$$

where $PB_{b,t}^{\text{clipped}}$ is the clipped BESS action. It was possible to clip the $a_{BESS,b,t} PR_{opt}$ term between $-PR_{opt}$ and PR_{opt} and introduce a penalty in the reward function if $PB_{b,t}^{\text{clipped}}$ is outside of its allowable range, but constraining the BESS action was believed to allow the algorithm to learn easier.

In the case of SAC, the actor network $\mu_{SAC}(s(t))$ will also output 17 actions but uses no activation. Instead, the actions are squashed with the tanh function and multiplied by the maximum amounts they are allowed to take on, before being clipped by the maximum generator output, the transmissible power of the lines at time step t, or the BESS limits to charge and discharge at time step t, for generators, transmission line flows, and BESSs, respectively. This is also expressed by equations (6.11), (6.12), and (6.13), but with $\epsilon = 0$.

In a single-agent setting to define the state, the normalized energy of every BESS, $E_{b,t}^{n}$, is calculated given the maximum and minimum state of charge, $SOC_{\max}$ and $SOC_{\min}$. The state can then be represented as an array of current conditions, including BESS energy, load at each bus, transmissible power, and time-step:

$$s(t) = [E_{4,t}^{n}, E_{5,t}^{n}, E_{6,t}^{n}, \widetilde{L}_{4,t}, \widetilde{L}_{5,t}, \widetilde{L}_{6,t}, \widetilde{R}_{t}, t/t_N]^T \tag{6.14}$$

where

$$\widetilde{R}_t = R_{l,t}/(\max_{l\in T_b, t\in H} R_{l,t}), \tag{6.15}$$

and

$$\widetilde{L}_{b,t} = L_{b,t}/(\max_{t\in H} L_{b,t}), \tag{6.16}$$

where t_N is the number of time steps in a single episode. Normalizing the battery energy and calculating the fractions of load, transmissible power, and time-step ensures the numbers remain small to speed up learning. Equation (6.1) can be rewritten as:

$$\delta_{b,t} = -L_{b,t} + G_{b,t}^{\text{clipped}} + (\eta_{\text{batt}})^k P B_{b,t}^{\text{clipped}} + \sum_{l\in T_b} P_{l,t}^{\text{clipped}}, \tag{6.17}$$

where $k = -1$ if BESS is charging, and 0 otherwise. At every time step t, the power balance must be satisfied at every bus b. The algorithm aims to train the agent to produce BESS action, line flow, and generation that would satisfy the power balance. Maximizing the absolute value of $\delta_{b,t}$ will then yield 0 in an optimal scenario. The reward $r_{b,t}$ at bus b and time step t can then be written as:

$$r_t = \sum_{b\in B} |\delta_{b,t} - \Lambda|, \tag{6.18}$$

where Λ is a positive constant representing the offset that controls the positive over-generation ensuring enough power is supplied to serve the load. Here we take $\Lambda = 0$. When forecasted load, $L_{b,t}^f$, and forecasted transmissible power, R_t^f, are taken into account in the state, the state definition becomes:

$$s(t) = [E_{4,t}^n, E_{5,t}^n, E_{6,t}^n, \widetilde{L}_{4,t}, \widetilde{L}_{5,t}, \widetilde{L}_{6,t}, \widetilde{R}_t, \widetilde{L}_{4,t}^f, \widetilde{L}_{5,t}^f, \widetilde{L}_{6,t}^f, \widetilde{R}_t^f, t/t_N]^T, \tag{6.19}$$

where the forecasted scaled loads are calcualted using equation (6.16).

6.3.2 Multi-agent Setting

In the multi-agent setting, N_{agents} output a pre-defined combination of generator, line flow, and BESS actions. Agent 1 outputs bus 4 BESS action, generator 1 action, line flows coming from bus 1, and $a_{LINE,\text{ bus 4}\rightarrow\text{ bus 5},t}$. Agent 2 outputs bus 5 BESS action,

generator 2 action, line flows from bus 2, and $a_{LINE,\text{ bus } 3\rightarrow \text{ bus } 5,t}$. Agent 3 outputs bus 6 BESS action, generator 3 action, line flows from bus 3, and $a_{LINE,\text{ bus } 5\rightarrow \text{ bus } 6,t}$. In this case, the reward vector is adjusted to accommodate individual rewards for each agent. The system was tested with three agents, each with the power balances from busses 1/4, 2/5, and 3/6 as rewards. This can be expressed as:

$$r_t = [|\delta_{1,t}| + |\delta_{4,t}|, |\delta_{2,t}| + |\delta_{5,t}|, |\delta_{3,t}| + |\delta_{6,t}|]^T. \tag{6.20}$$

When forecasted actions are involved, the same procedure as in the single-agent setting is used. In both multi-agent and single-agent settings, the replay buffer W does not pick random samples of N_s but instead picks a batch N_s of samples as they appear in sequence to help the algorithm learn the transition dynamics.

6.4 Experimental Setup

The neural network architectures used for DDPG and SAC critic and actor networks are shown in Figures 6.3, 6.4, and 6.5. $SOC_{\max}$ and $SOC_{\min}$ are chosen to be 20% and 80%, respectively. Hourly ambient temperature, wind speed, wind direction, and solar irradiance data was obtained from the BADC dataset and the maximum ambient temperature for each of the 4 seasons was used in the calculation of the ampacity [41], which was done using the IEEE 738 standard [50]. Lithium Nickel-Manganese Cobalt BESS was assumed with calendric aging and cyclic aging constants found in [37]. Drake conductor was assumed with 138kV lines in the 6-bus test grid. Twenty three steps were simulated, and 12 time step inputs were used in forecasting load and transmissible power. The modified 6-bus test grid was supplemented with varying bus loads. The loads for busses 4, 5, and 6 were taken from the corresponding IEEE 24-bus test grid [49] loads for busses 1, 2, and 3. The generator maximum values for generators at busses 1, 2, and 3, were taken to be 50 MWs, 60 MWs, and 50 MWs, respectively. At the start of each simulation episode, the BESS capacity was assumed to be at 80% of the calculated BESS capacity. NLP optimization was

performed using the Gurobi solver with neural network training using TensorFlow modules. The hyper-parameters for DDPG and SAC algorithm training are shown in Table 6.2.

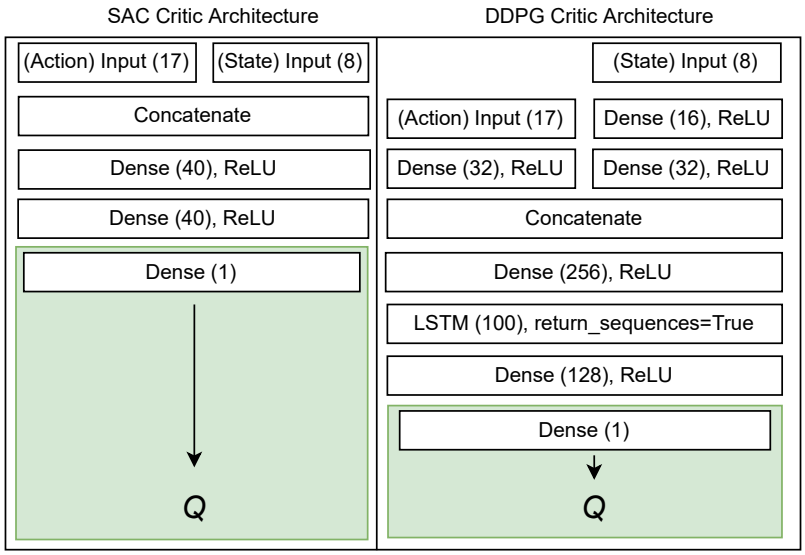

Figure 6.3: DDPG and SAC critic network architectures.

6.5 Results and Discussion

The optimal BESS capacity and power rating were calculated to be 1042 MWh and 73 MWs, respectively. The cumulative episodic reward is calculated according to equation (6.17) as the sum of 6 bus power balances over 24 hours. To calculate the power balance per bus per hour $[u] = [\text{MW}/(\text{bus} \cdot \text{hour})]$ we divide the cumulative episodic reward by $24 \cdot 6$ [hour $\cdot$ bus]. We use this metric to compare the performance of algorithms against each other. The learning curves without load and ampacity forecasting and with load and ampacity forecasting are shown in Figure 6.6 and Figure 6.7, respectively. The training of each model using one of DDPG, SAC, MADDPG, and MASAC algorithms, for cases with and without load forecasting, took approximately 1 day using a 3.30 GHz 125 Gigabyte RAM 10-core Intel Core i9-9820X CPU virtual machine. Training the load and ampacity forecast models took approximately 1 hour

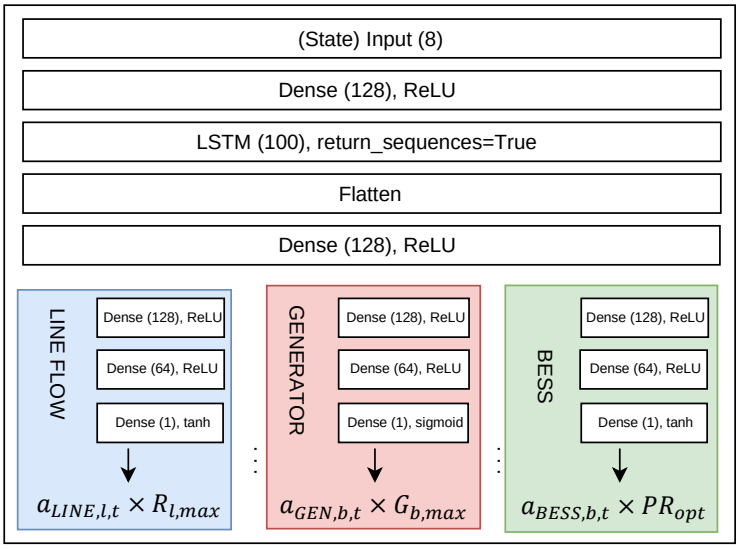

Figure 6.4: DDPG actor network architecture.

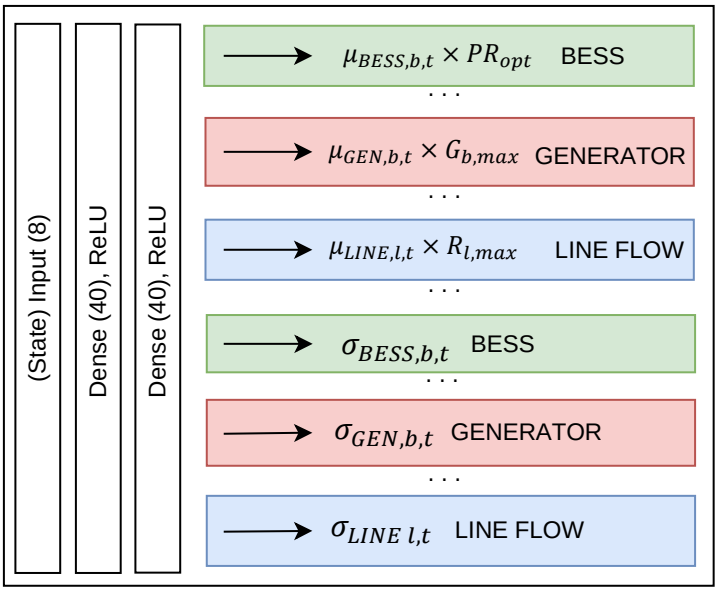

Figure 6.5: SAC actor network architecture.

per model per hyper-parameter setting using a Tesla V100 GPU on the same virtual machine. Grids with a higher number of buses will require more training time if the same hardware is employed. After the models are trained and run in real-time, the desired quantities are calculated virtually instantaneously.

From Figure 6.6 we can see that while the SAC algorithm achieves the highest cumulative episodic reward, the learning becomes unstable after about 7500 episodes. Zooming in on Figure 6.6, we can observe the learning of the algorithms in the stable regions shown in the right hand side of Figure 6.6. As can be seen in Table 6.3, when forecasting is not involved in the definition of the state as per equation (6.14), SAC performs best with the highest cumulative reward of -5.48 [u], followed by DDPG, with -7.66 [u]. SAC converged after around 1200 episodes, whereas DDPG converged at about 2700 episodes. Interestingly, both SAC and DDPG converged around a similar value between 6 [u] and 8 [u]. Multi-agent versions of both algorithms under-performed their single-agent counterparts, with MASAC converging to an average value of -132.8 [u] in about 5000 episodes while MADDPG under-performed with an average value of -83.9 [u] in approximately 4000 episodes.

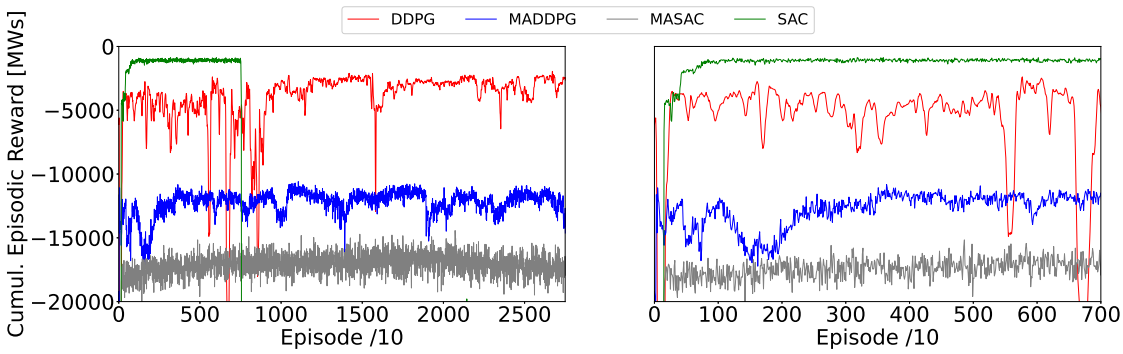

Figure 6.6: Algorithm convergence without load and ampacity forecasting. Stable region on the right.

SAC achieved the highest cumulative episodic reward, learning is unstable after about 12500 episodes as can be seen in Figure 6.7. We can observe the performance of the algorithms in the stable region, by zooming in on the right hand side of Figure 6.7.

When forecasting is involved, as per equation (6.19), SAC again outperformed other algorithms with the highest cumulative episodic reward of -6.20 [u] and converged around the value of -9.70 [u] in approximately 2500 episodes. DDPG performed much worse at the best value of -609 [u], converging around 2000 episodes, while MASAC converged to a value of -289 [u] with the best performance of -241 [u] in approximately 200 episodes. MADDPG had better convergence properties reaching about -77.2 [u] in about 250 episodes.

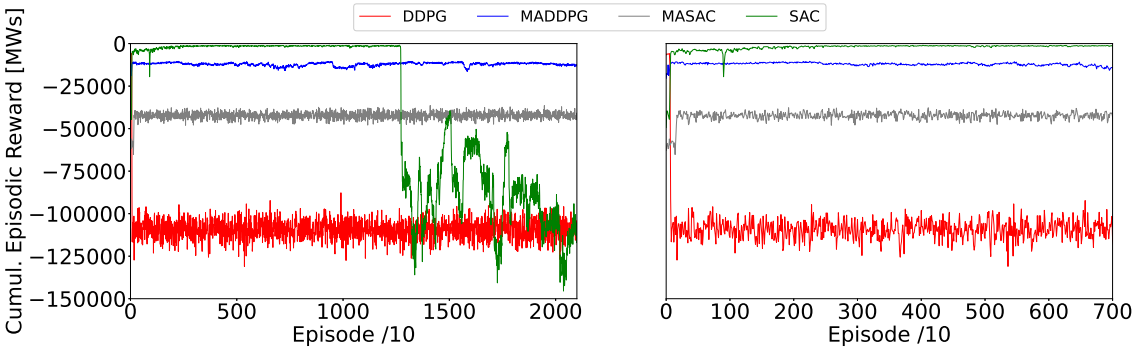

Figure 6.7: Algorithm convergence with load and ampacity forecasting. Stable region on the right.

It appears single-agent algorithms outperformed their multi-agent versions, most likely because multiple neural networks added additional complexity to the problem. Forecasting seems to provide no beneficial effect towards improving the final result of the algorithms or their speed of convergence.

Given the relative performance of SAC compared to the other algorithms, we increased the over-generation constant Λ from 0 to 10 MW. We also modify the actor network loss to match the PINN loss stated in equation (6.10). We can observe that allowing the algorithm to learn to over-generate improved the best cumulative reward to -2.70 [u] and the average cumulative reward to -4.93 [u], while SAC with PINN produces the best cumulative reward of -5.07 [u] and the average cumulative reward of -6.77 [u]. SAC with $\Lambda = 10$ MW also produces the most stable learning among the three. The resulting cumulative episodic reward curves are shown in Figure 6.8.

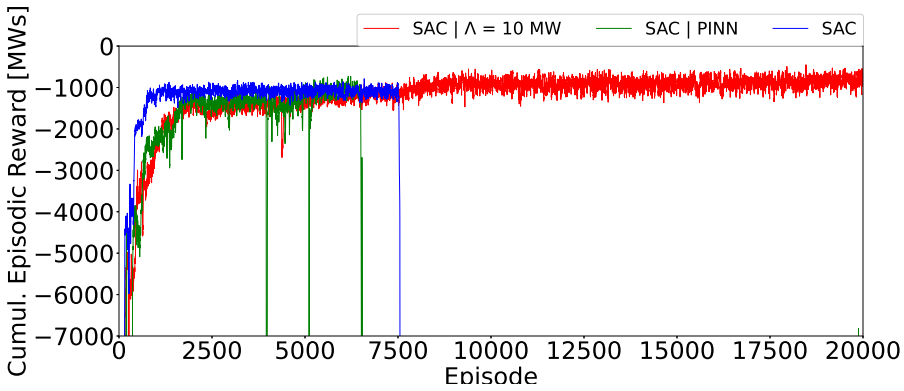

Figure 6.8: SAC, SAC with PINNs, and SAC with $\Lambda = 10$ MW.

With over-generation, equation (6.17) can be used to compute the histogram for power balance for every bus. When we compute this for bus 1 the mean of the distribution is 9.29 MW, close to the expected 10 MW. The histogram showing the power balance for bus 1 is shown in Figure 6.9, where positive mean implies that on average, the actor over-generates.

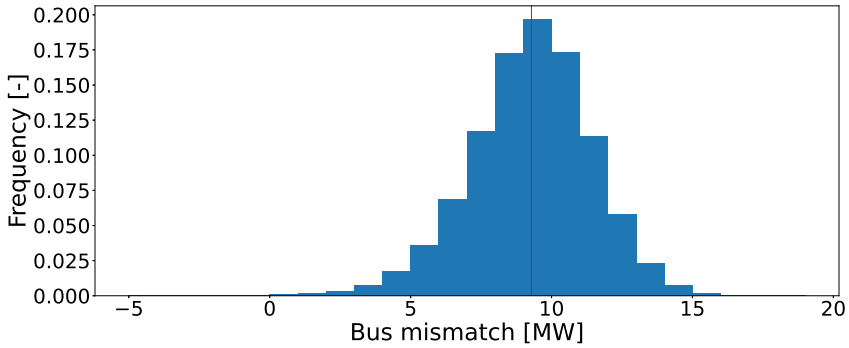

Figure 6.9: Error distribution for bus 1.

When we calculate the means for power balances for other busses, we can see that buses 1-5 have positive means, meaning in most cases the load is met, while bus 6 has negative mean, and in some cases load is not completely met. Bus 6 has the worst average mean power balance at -5.28 MW. The means of the power balance for other busses are shown in Table 6.4.

The non-linear programming (NLP) method is used to calculate the optimal BESS performance. Since the BESS capacity and the BESS power rating are known, we re-ran the NLP method in Section 6.2.1 but define the BESS capacity and power rating. The objective function was chosen to be minimizing BESS action, which is expressed as:

$$\min \sum_{b} \sum_{t<N} (|PB_{b,t}^{\text{char}}| + |PB_{b,t}^{\text{dischar}}|), \quad b \in B, \tag{6.21}$$

where N is the number of time intervals Δt. We can compare the BESS energy calculated using the NLP method and using SAC with PINN at $\Lambda = 10$ MW. We can see that the energy of the BESS at bus 5 decreases monotonically but at a slower rate than predicted by the NLP method. The energy level of the BESS at bus 5 calculated with a trained actor is shown in Figure 6.10.

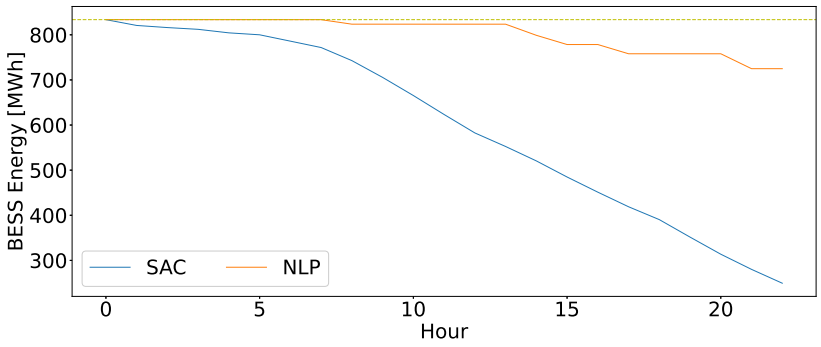

Figure 6.10: Energy of BESS at bus 5.

We can also calculate the power through the lines, the bus power balance, and the BESS output power entering every bus. For bus 5, the power balance is positive, signifying the actor over-generates ensuring all load is met. The power through the line, the BESS output power, and the power balance for bus 5 are shown in Figure 6.11.

6.6 Conclusion

This paper presents the application of DRL algorithms, in single- and multi-agent settings, to forecast BESS, line flow, and generator actions for a modified IEEE 6-bus

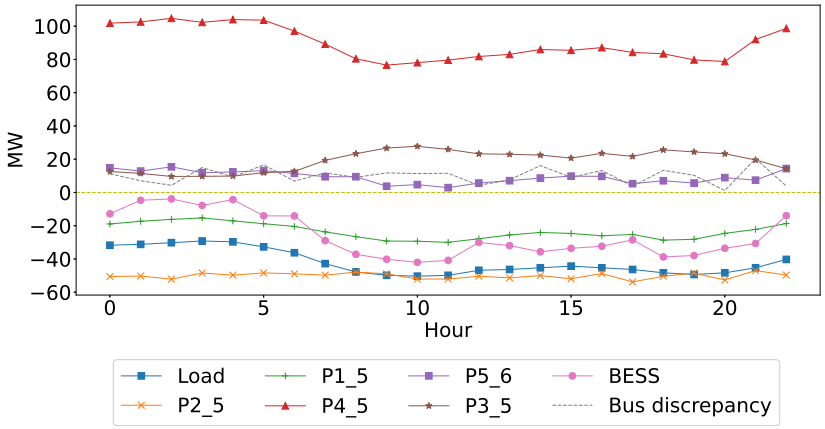

Figure 6.11: Power flow over lines and BESS power at bus 5.

test grid. The standard test grid was adapted to consider the combined application of DTLR with utility-scale battery storage as a solution to improve the use of transmission systems. This approach can be used, for example, to increase the current-carrying capacity of the systems and defer the construction of new lines.

The performances of DDPG, MADDPG, SAC, and MASAC algorith are compared, with SAC outperforming the other methods based on both the accuracy of the solution and the speed of convergence. As the main result, SAC achieved the best bus power balance of - 5.48 MW/(bus·hour), on an hourly average. DDPG presented the second-best result with - 7.66 MW/(bus · hour). Their multi-agent versions reached several times higher values, indicating that they are not suitable for this application. When overgeneration of 10 MW was introduced, the best power bus balance improved up to -2.70 MW/(bus · hour). The introduction of the physics-informed neural network loss function and 1-step forecasting of load and transmissible power were also considered, and it was found that their introduction does not affect the convergence and the best bus power balance during learning.

Finally, the authors suggest as future work that the effect of multi-step forecasting on the performance of the algorithms can be explored, the reward function can be modified to enable more accurate learning, and the clipping for BESS action can be

changed to include a penalty. In addition, SAC and other continuous state and action algorithms can also be tested on larger test grids.

Table 6.1: Summary of recent studies on BESS control using RL.

Study	Algorithm	Control Area	Problem	Objective
[69]	SAC, DDPG, DDQN	Microgrid	Power plant control	Cost minimization
[70]	TD3, DDPG	2 area control	PID control	Area control error minimization
[81]	SAC, DDPG, DDQN	3 area control	Frequency control	Generation cost, battery aging cost, unscheduled interchange cost
[82]	TD3, SAC, DDPG, DQN, A3C, PPO	Microgrid	Frequency control	Fuel consumption minimization
[76]	MADDPG	IEEE 123-bus test grid	Voltage control	Voltage deviation minimization
[75]	MASAC, MATD3, SAC	IEEE 123-bus test grid	Voltage control	Voltage deviation and curtailment minimization
[67]	SAC, TD3, DDPG	Microgrid	EV charging	Load and peak load minimization
[83]	DDQN	Microgrid	Microgrid management	Charging cost minimization

Table 6.2: Hyper-parameters used in the algorithms.

	SAC/MASAC	**DDPG/MADDPG**
Exploration γ	0.7	0.9
polyak τ	0.1	0.1
Buffer size	1000000	200000
Batch size	128	64
Actor learning rate	0.001	0.002
Critic learning rate	0.001	0.001
Optimizer	Adam	Adam
Entropy α	0.9	N/A
Regularization ξ	0.001	N/A

Table 6.3: Algorithm Performance on BESS Action Prediction

	No Forecasting [u]		**Forecasting [u]**	
Algorithm	***Best***	***Average***	***Best***	***Average***
DDPG	-7.66	-9.89	-609	-708
SAC	-5.48	-7.31	-6.20	-9.70
MADDPG	-73.6	-83.9	-72.3	-77.2
MASAC	-96.4	-132.8	-241	-289

Table 6.4: Mean Bus Power Balances

Busses	***1***	***2***	***3***	***4***	***5***	***6***
Mean Power Balance [MW]	9.29	9.19	9.35	9.38	0.36	-5.28

Chapter 7

BESS Sizing and Evaluation

7.1 Introduction

Introduction of battery energy storage systems (BESSs) into utility-scale transmission grid has the potential to dramatically increase the level of penetration of renewable energy assets and defer the construction of new transmission lines [32]. Proper sizing of the capacity of BESS is then crucial to efficient and cost-effective investment for any company. Size of BESS capacity is influenced by loads at substations, the power-carrying capacities of the adjacent transmission lines, and the acceptable depth-of-discharge (DOD) of the BESS.

When a BESS is placed at a substation, and the configuration of the near-by connections to that substation is not radial, BESS has the potential to defer the construction of new transmission lines, by discharging energy to alleviate the load in times when the power-carrying capacity of the transmission lines is limited [84]. The transmission lines were designed to operate at a maximum temperature. When the current passes through the transmission line it heats up the metal, which, if the temperature is too high, can cause the metal to anneal [85]. The internal temperature of the conductor varies with the type of the conductor, as well as with external weather conditions, such as, ambient temperature, wind speed, wind direction, solar irradiance, and precipitation, of which wind speed and direction has the highest impact [33] This internal temperature can then be used to calculate the maximum

amount of current in Amperes that can be passed through the conductor. This dynamic amperage of the transmission lines is referred to as Dynamic Thermal Line Rating (DTLR). However, for planning and reliability purposes the DTLR of the transmission lines is assumed to be constant and is chosen conservatively, being varied with the seasons. This is referred to as Static Line Rating (SLR). In practice, DTLR can be multiple times higher than SLR, which means that using DTLR in real time operations has the potential to distribute power in the grid more efficiently [84]. We present here a general methodology for sizing BESS capacity taking into account transmission line outages, DTLR, load growth, and BESS degradation. We then apply this methodology to real-life data from a distribution substation in Alberta, Canada.

However, sizing the BESS quantitatively is generally not enough to determine the most appropriate BESS capacity for the situation. Depending on the application, the owner of the BESS would weight different aspects of BESS operation to determine the most suitable BESS capacity, taking into account metrics pertaining to the situation.

We therefore present a practical guide to sizing BESS for the owner of transmission assets in the transmission deferral application based on the metrics of unserved energy, total unserved energy, duration of unserved energy, total duration or unserved energy, and service life. Additionally, we present a proposal to extend the BESS service life by moving it between substations in a transmission deferral application. Moving the BESS between different locations can extend the service life of the BESS provided the load at the target substation is lower.

This work is organized as follows. Section 7.2 covers recent developments in BESS sizing. Section 7.3 introduces the linear programming-based, and grid-search based sizing methods. Section 7.4 explains the data set and assumptions. Section 7.5 presents the evaluation methods and Section 7.6 discusses the results.

7.2 Related Work

Liu et al. [86] integrate the BESS with the wind farm to present a novel method for BESS sizing using a dynamic programming method. Capacity degradation is taken into account and together with operating costs is used as an objective. Hesse et al. [37] calculate the capacity of a single BESS in a household considering the presence of photovoltaic (PV) panels by employing mixed-interger linear programming (MILP) with the objective of minimizing operating cost. BESS degradation is calculated by linearizing calendric aging and total aging is calculated as a superposition of cyclic and calendric aging as presented in Martins et al. [39]. Galeela et al. [46] size BESS on 24-bus IEEE RTS taking into account outages and DTLR and employ sequential Monte-Carlo runs together with MILP to size BESS by minimizing the operating on each time step. Similarly, Metwaly et al. [41] size BESS capacity on an individual time step using MILP and considering the presence of wind turbines at the locations of the loads on the 24-bus RTS. Wind speeds are simulated using an ARMA model and the study considers transmission line outages and DTLR. Vrettos et al. [43] utilize a Genetic Algorithm (GA) approach to size the BESS, PV installation, and wind turbine capacity using the levelized cost of energy in the fitness function. The method was shown to increase the penetration of renewable energy sources from 20% to 60%. Liao et al. in [87] uses electron drifting algorithm for the sizing of BESS capacity and PV inverter operation and compares different electricity tariffs to determine its impact on BESS investment. Dual-loop algorithm is proposed with the inner loop performing the scheduling and the outer loop performing the sizing. Wong et al. in [88] use Whale Optimization Algorithm for optimal sizing and placement of BESS in a distribution grid. The algorithm achieves comparable performance with Particle Swarm Optimization (PSO) and and Firefly Algorithm based on the reduction of power losses. Alhumaid et al. in [89] size BESS by minimizing the cost using multi-input non-linear programming assuming the presence of solar and wind turbines in

a 24-bus RTS for different energy mixes. Sodium-sulfur in combinations with hybrid solar-wind energy mix was found to be most cost-effective. Boonluk et al. in [90] apply GA and Particle Swarm Optimization to the sizing and positioning of BESS in IEEE 33-bus distribution system with the aim of minimizing the cost associated with power losses, voltage deviations, and peak demand. Using the BESS resulted in lower costs compared to the case without the BESS.

This work sizes BESS considering simulated transmission line outages, BESS degradation, and DTLR, and presents an evaluation method to select appropriate BESS capacity and power rating given the constraints from the transmission line utility provider. We describe a non-linear programming-based (NLP) sizing methodology and extend BESS degradation into a grid-search approach.

7.3 System Model

The system is sized using two methods, a linear-programming-based approach, and a grid search approach. Grid search approach is easier to implement but requires assumptions about BESS operation, while linear-programming-based methods require no assumptions about BESS control methodology but may require unrealistic amounts of time to finish. The two methods serve to validate each other.

7.3.1 Linear Programming

Section 4.3 presents the BESS capacity sizing methodology.

7.3.2 Grid Search

Grid search BESS capacity sizing method involves assuming BESS capacity and BESS power rating are known, and then calculating the amount of unserved energy based on those. The BESS capacity and BESS power rating are assumed small at the beginning, and are then increased by a specified threshold until the amount of unserved energy is reduced to 0. A combination of the smallest BESS capacity and BESS power rating

that result in 0 unserved energy are assumed to be the minimum BESS capacity and power rating necessary.

In order to run the grid search simulation the operating strategy of each BESS considered needs to be specified. This is because the simulation updates the values of capacity, SOH, cyclic and calendric aging forward based on the BESS charging and BESS discharging amounts. Specifying the BESS operating strategy does not guarantee that BESS capacity calculated using linear programming method will be enough in case with multiple busses, but does hold true when a single BESS is present. The formulation below will consider only a single BESS.

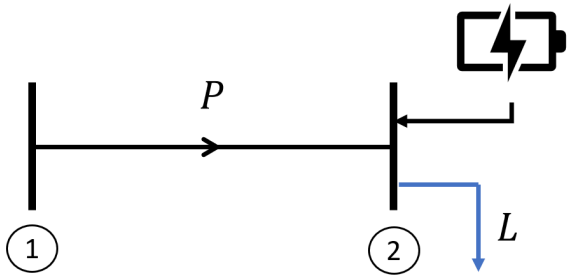

Figure 7.1: 2-bus setup for BESS grid search

The BESS energy is updated as previously stated in (4.5). The BESS operating strategy assumed here is that BESS will recharge whenever it can and discharge whenever it has to.

From Figure 7.1 the balance of power at bus 2 is:

$$-L_{t,2} - PB_{t,2}^{\text{char}}/\eta_{\text{batt}} + \eta_{\text{batt}} PB_{t,2}^{\text{dischar}} + P_{t,2} = 0 \tag{7.1}$$

at time t. Since the BESS capacity at time step t is given by (4.6) and BESS cannot charge and discharge at the same time, (7.1) used in tandem with (4.6) can be used to determine whether the BESS needs to charge or discharge.

When $P_{t,2} - L_{t,2} > 0$ and $E_{b,t} \leq SOC_{\min} E_{\text{opt}}$, the BESS can recharge according to:

$$PB_{b,t}^{\text{char}} = \min(PR_{\text{opt}}, \frac{SOC_{\max} E_{\text{opt}} SOH_{b,t} - E_{b,t}(1 - \frac{SD_{\text{batt}}}{d})}{\eta_{\text{batt}} \Delta t}, P_{t,2} - L_{t,2}) \tag{7.2}$$

and $PB_{b,t}^{\text{dischar}} = 0$. However, if $E_{b,t} = SOC_{\max} E_{\text{opt}}$, $PB_{b,t}^{\text{char}} = 0$ and $PB_{b,t}^{\text{dischar}} = 0$.

When $P_{t,2} - L_{t,2} < 0$ the load is higher than the power from the grid. When $E_{b,t} - SOC_{\min} E_{\text{opt}} > 0$ the BESS is forced to discharge according to:

$$PB_{b,t}^{\text{dischar}} = \min(PR_{\text{opt}}, \eta_{\text{batt}}(E_{b,t}(1 - \frac{SD_{\text{batt}}}{d}) - SOC_{\min} E_{\text{opt}})/\Delta t, L_{t,2} - P_{t,2}) \tag{7.3}$$

and $PB_{b,t}^{\text{char}} = 0$. The unserved energy of the BESS, $P_{\text{unserved},\,t}$, is the energy that a BESS must provide, but is unable to, in a given time interval. It is the difference between the energy that needs to be supplied and the energy that is actually supplied, at time step t, and is expressed as:

$$P_{\text{unserved},\,t,2} = |\max(0, L_{t,2} - P_{t,2} - PB_{2,t}^{\text{dischar}})|. \tag{7.4}$$

The unserved energy, $P_{\text{unserved},D,2}$, for a time period length D, is then the sum of the unserved energies for time periods $t \leq D$ and is expressed as:

$$P_{\text{unserved},D,2} = \sum_{t \leq D} P_{\text{unserved},\,t,2}. \tag{7.5}$$

Using grid search method, the objective then, is to find the smallest BESS capacity, such that total unserved energy is 0. This problem is summarized as:

$$\min E_{\text{opt}} \quad \text{s.t.} \sum_{t \leq D} P_{\text{unserved},\,t,2} = 0. \tag{7.6}$$

To do this in practice, the BESS capacity is chosen, and a calculation of the unserved energy is made, over the time interval D. If the unserved energy is greater than 0, then the BESS capacity is increased, and the calculation of the unserved energy is made again, until the unserved energy is 0.

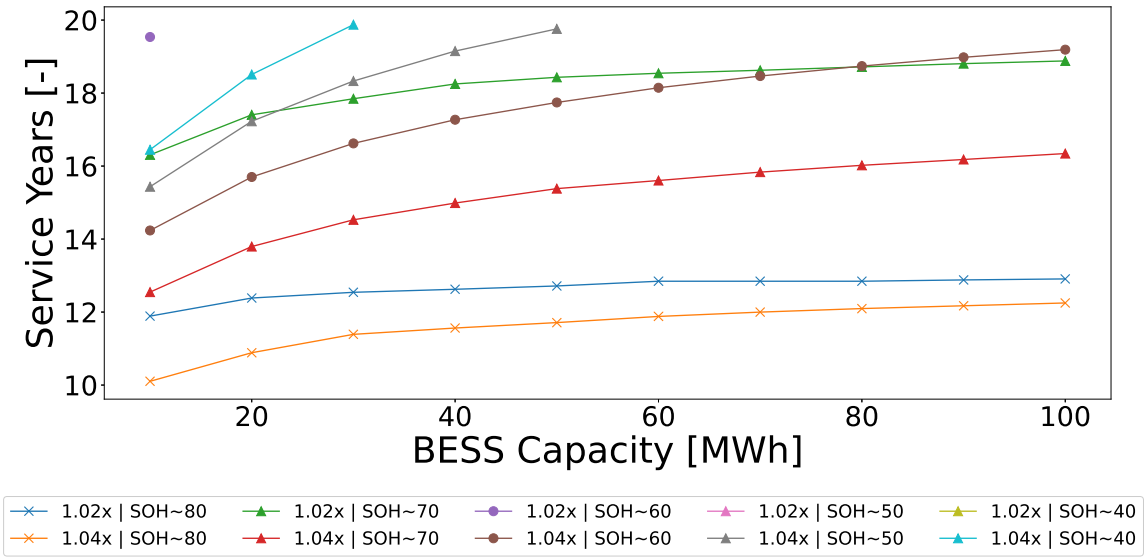

Figure 7.2: Service life and BESS capacity for different load increases.

7.4 Experimental Setup

The BESS in the analysis is lithium-nickel-manganese-cobalt (NMC) in composition. For BESS degradation calculations, the values found in [37] were used. The calculations of the ampacity were then performed using the IEEE-738 standard [50]. A weather station located in the vicinity of the transmission line was used to collect data on ambient temperature, wind speed, wind direction, and solar irradiance, in 1-minute intervals. The maximum discharging of the BESS was taken to be no less than 20% of the optimal capacity and the maximum charging was taken to be no more than 80% of its optimal capacity. The initial energy capacity of every BESS at the start of the simulation interval was set to equal 80% of the optimal BESS capacity.

7.5 Evaluation

If the capacity or power rating is too low, then throughout the BESS service life some energy will not be delivered as needed. To calculate this energy, whenever a BESS cannot supply the entire amount of energy it has to, the amount that cannot be served is recorded. The maximum amount of energy that cannot be served is 0.

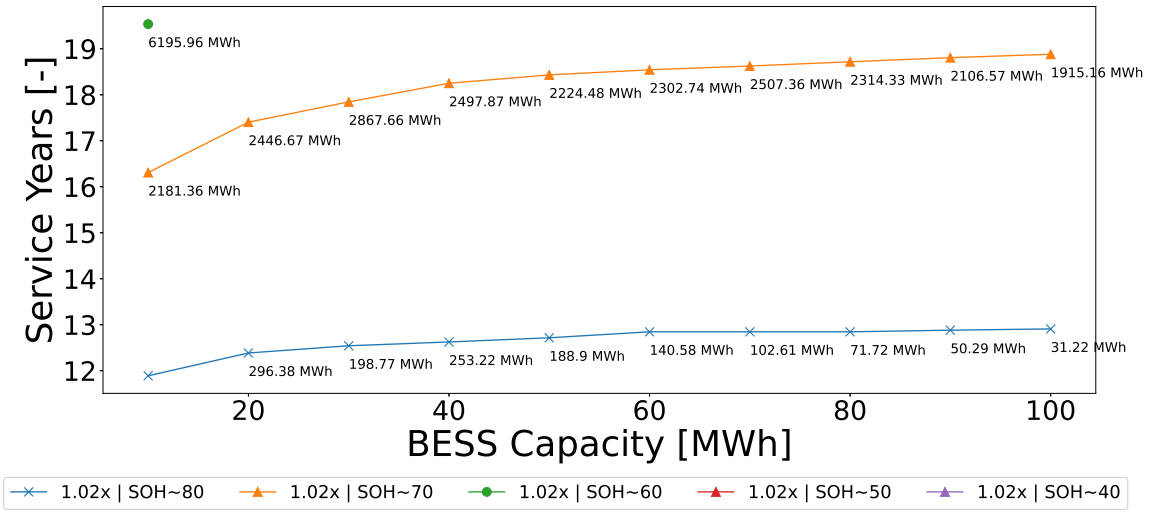

Figure 7.3: Service life and BESS capacity for 2 percent load increases.

Service life and capacity curve can be used by the transmission utility to determine the useful life of the BESS considering the level of SOH they want the BESS to get to. Nominal BESS capacities are used in the following curves for clarity and easy-comparison reasons. Figure 7.2 shows the service life of BESS and the installed BESS capacity for 2% and 4% load increases. This curve shows the number of service years the BESS served when it reached a particular state of health level (here 40, 50, 60, 70, and 80%). When we consider 80% as the end of the service life for 2% load increase per year, the curve has a plateau starting at around 30 MWh capacity. Past 30 MWh BESS capacity, an insignificant amount of service life is added compared with the increase in BESS capacity required.

Figures 7.2 - 7.9 assume sufficient power rating is present to ensure all load is met based on the BESS inverter capacity. Figure 7.3 shows the unserved energy in MWh once 70% or 80% SOH is reached. Load is kept constant at 2% increase. Service life is higher when the eventual SOH reached is lower, as shown. Only 2 curves, and a single point are shown in Figure 7.3 because the BESS never reached SOH levels below 60%. The unserved energy generally decreases with increasing BESS capacity, but because the unserved energy is taken at the time the SOH is reached, the unserved energy does not have to decrease monotonically. In both curves a plateau is indicating

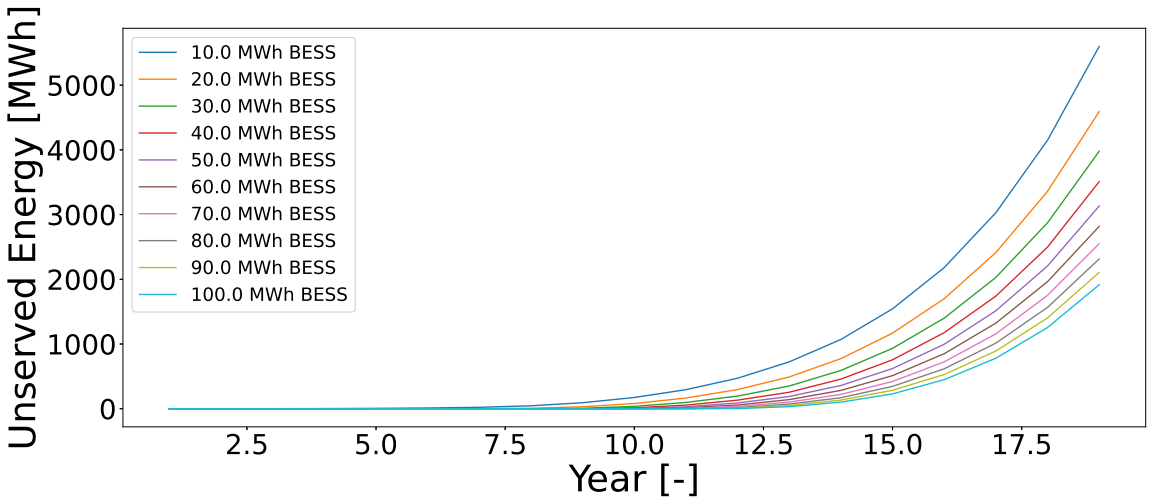

Figure 7.4: Unserved energy and service life for different BESS capacities.

insignificant gain in service life against the increase in BESS capacity.

Figure 7.4 shows the total unserved energy at the end of each year of the service life for different BESS capacities. The total unserved energy monotonically decreased for larger BESS capacities. This curve can be used to judge how much energy is unserved during every year of the BESS operation with the particular BESS, and can then be compared against a predefined metric. A significant divergence between the unserved energies for different BESS capacities starts around 7.5 years of service. At certain number of service years BESS capacities result in unserved energy. If we zoom in on Figure 7.4, unserved energy starts to appear at different service years, with the service years increasing with growing BESS capacity, as shown in Figure 7.5. 40/50 MWh BESS, 60/70 MWh, and 80/90/100 MWh groups of BESS capacities result in unserved energy starting from the same number of service years.

Similarly to calculating the amount of unserved energy, the duration of events when energy is not served can also be estimated. The duration of unserved energy events is important to transmission utility companies because it signifies the duration of time that customers may be on an outage, given a particular BESS capacity. Unserved energy is calculated as the sum of the unserved energies over the service life. The real cost of an unserved energy event can be much higher than the energy price per MWh

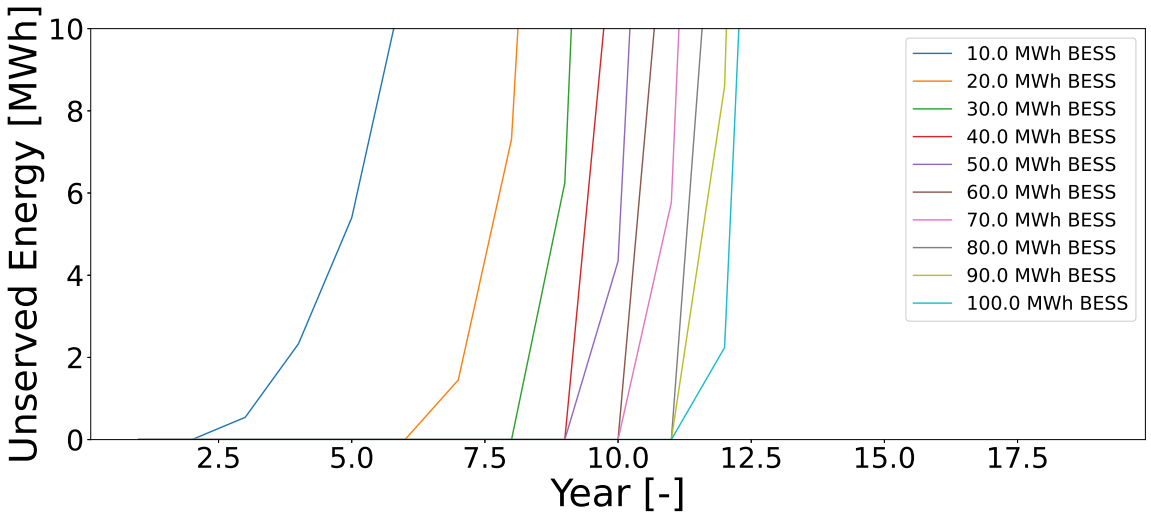

Figure 7.5: Unserved energy and service life for different BESS capacities, closer view.

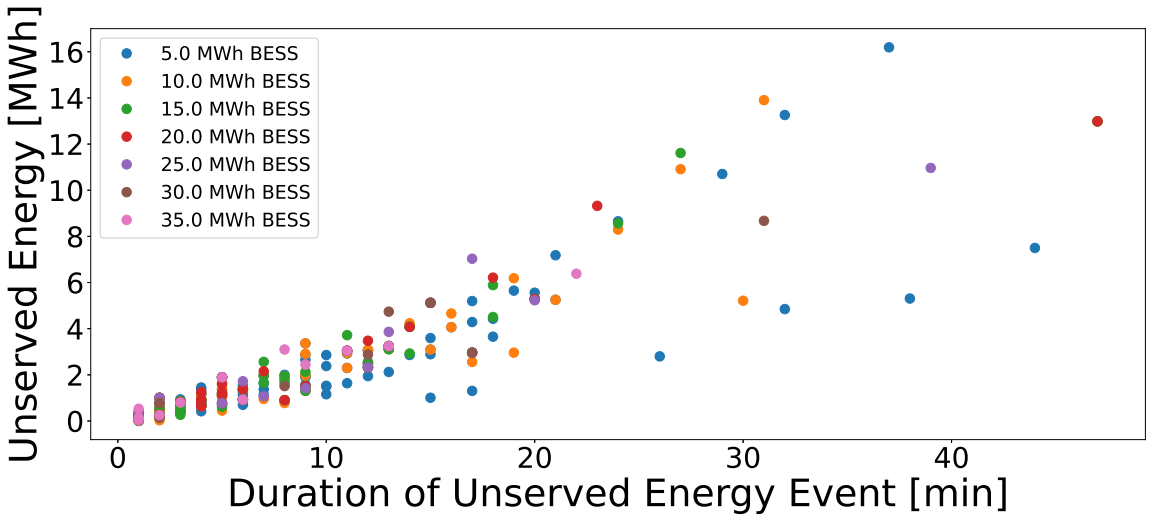

Figure 7.6: Unserved energy and duration of unserved energy events for different BESS capacities.

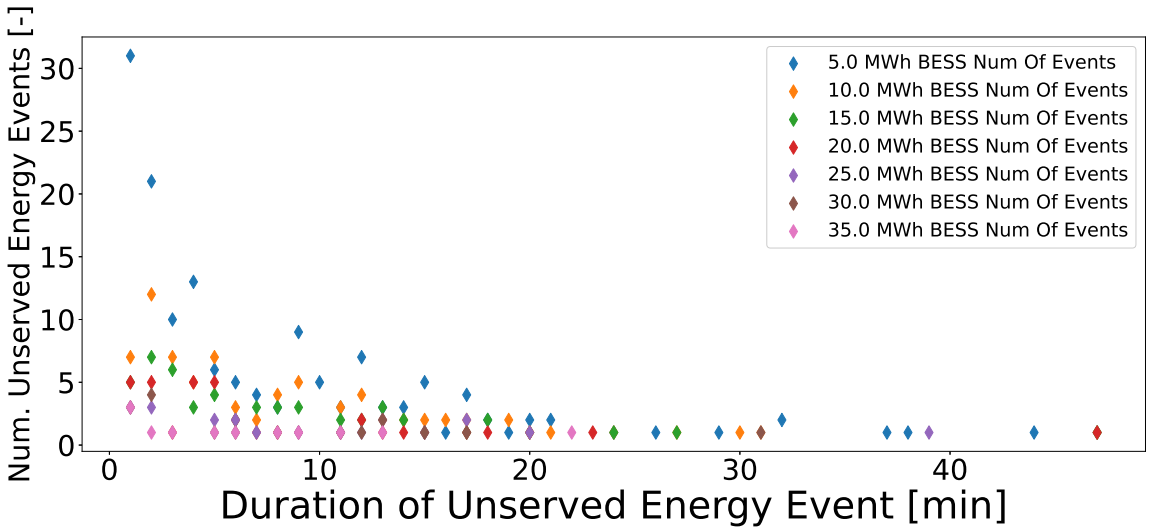

Figure 7.7: Number of unserved energy events and duration of unserved energy events for different BESS capacities.

and different companies may have a different cost associated with unserved energy duration events. The unserved energy and the duration of unserved energy events over a 10-year span are shown in Figure 7.6. Smaller BESS capacities experience larger unserved energy event counts and longer unserved energy event durations. The number of unserved energy events, as well as the duration of those events decreases with increasing BESS capacity, as shown in Figure 7.7. The number of unserved energy events is an important indicator of BESS usefulness because each unserved energy event represents an outage that some of the loads on the system, homes or industrial loads, may be experiencing. Duration between unserved energy events is important because it shows how quickly the BESS is able to recharge and supply the necessary power to the grid. The farther away are the unserved energy events the more robust is the performance of the BESS given the capacity and power rating. Figure 7.8 shows the durations between unserved energy events and the unserved energy events count for increasing capacities for a 10-year span. The duration increases for larger BESS capacities and is smaller for smaller BESS capacities.

Figure 7.9 shows the total amount of unserved energy that was experienced by each BESS over a 10-year period and it also shows the fraction of the amount of unserved

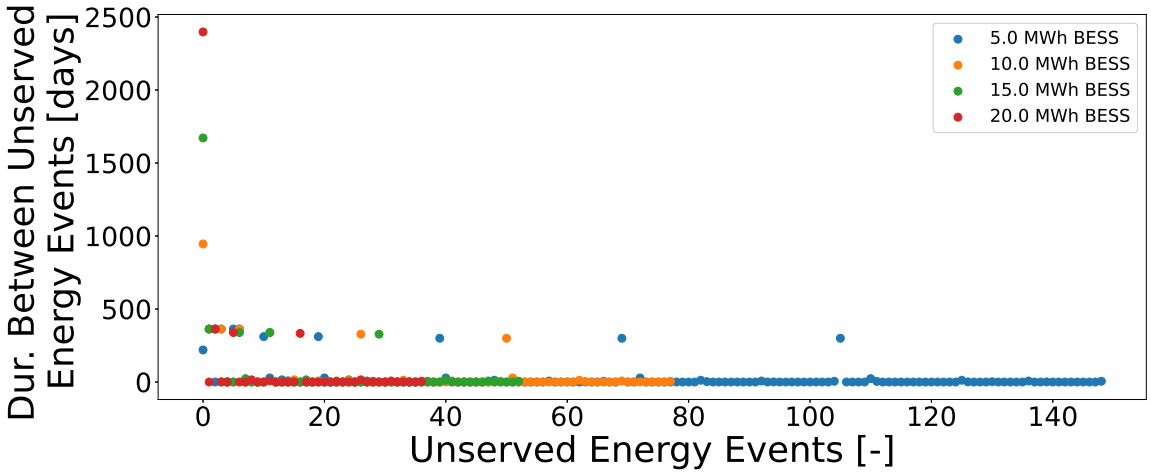

Figure 7.8: Duration between unserved energy events and unserved energy events for different BESS capacities.

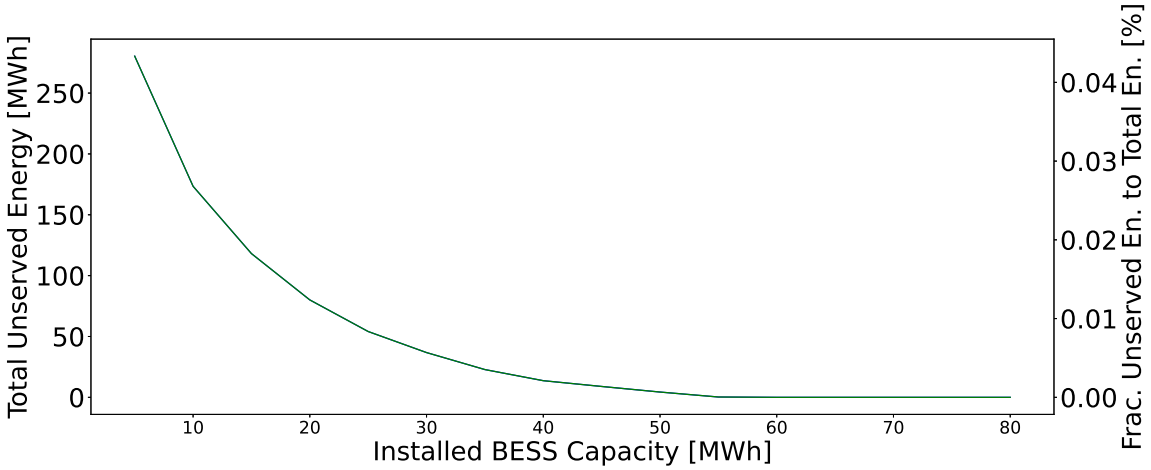

Figure 7.9: Total unserved energy for different BESS capacities.

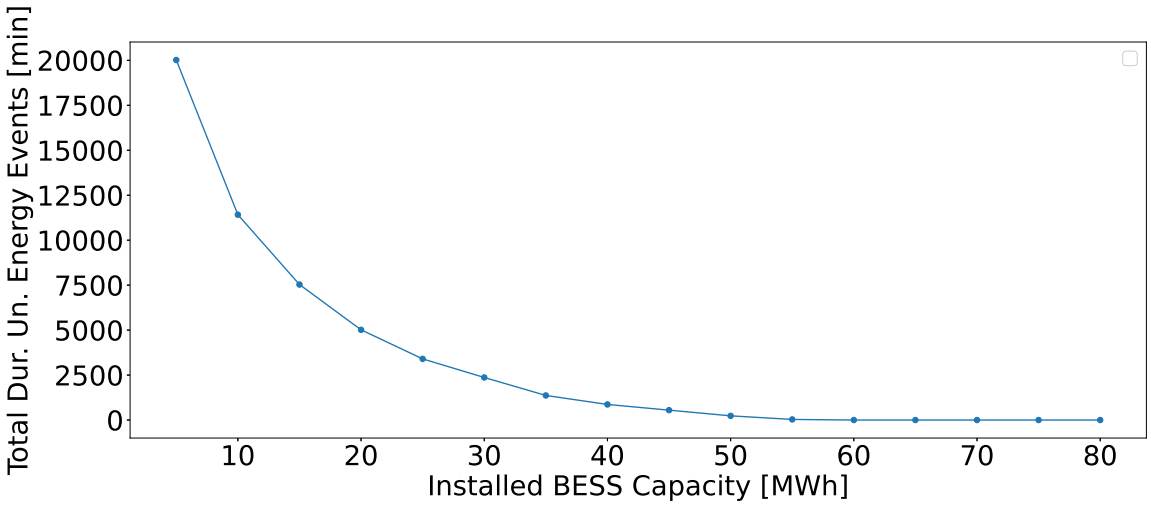

Figure 7.10: Total duration of unserved energy events for different BESS capacities.

energy to the total amount of BESS served energy over the 10-year period. This shows that as the BESS capacity increases the fraction of unserved energy decreases. Unserved energy is calculated as the sum of the unserved energies over the service life, as shown in equation (7.5). With larger BESS capacity, the total amount of unserved energy decreases. A plateau begins around 45 MWh, when the total unserved energy decreases much slower against the increase in BESS capacity. The unserved energy here is made up of unserved energy cases where non-zero unserved energy is always added during the course of the service life of BESS. This energy then must monotonically decreases for increasing BESS capacities. Total amount of unserved energy can be used as a criteria by the transmission utility looking to minimize the amount of unserved energy the system generates. Figure 7.10 shows the total duration of unserved energy events over a 10-year period. With larger BESS capacity, the total duration of unserved energy events decreases. A plateau begins to occur around 45 MWh, when the total duration of unserved energy events decreases much slower compared with the increase in BESS capacity. This curve is an agglomeration of Figure 7.6. Total duration of unserved energy can be used as a tool to look at the performance of the BESS over a 10-year service life by utility companies looking to minimize the total duration of unserved energy events and setting a criteria to determine the necessary

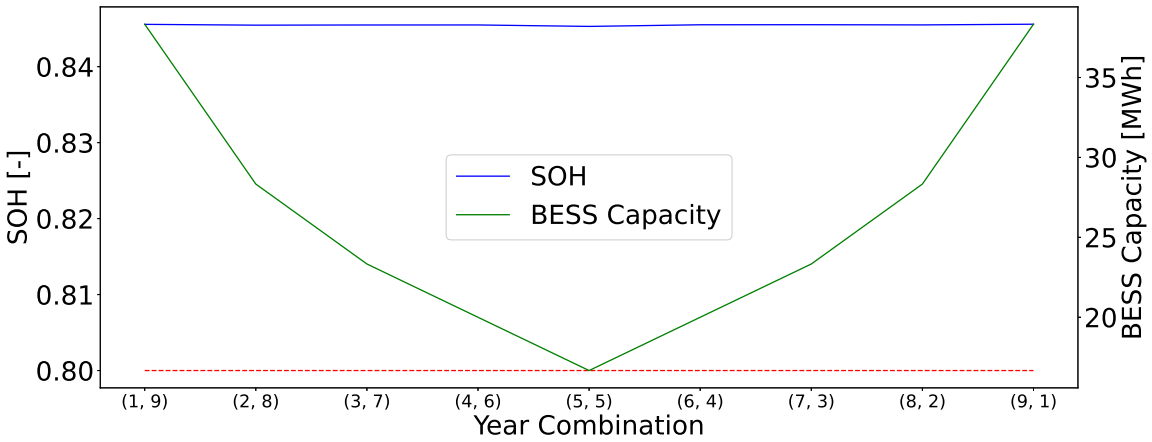

Figure 7.11: Capacity of BESS as a function of the year combination.

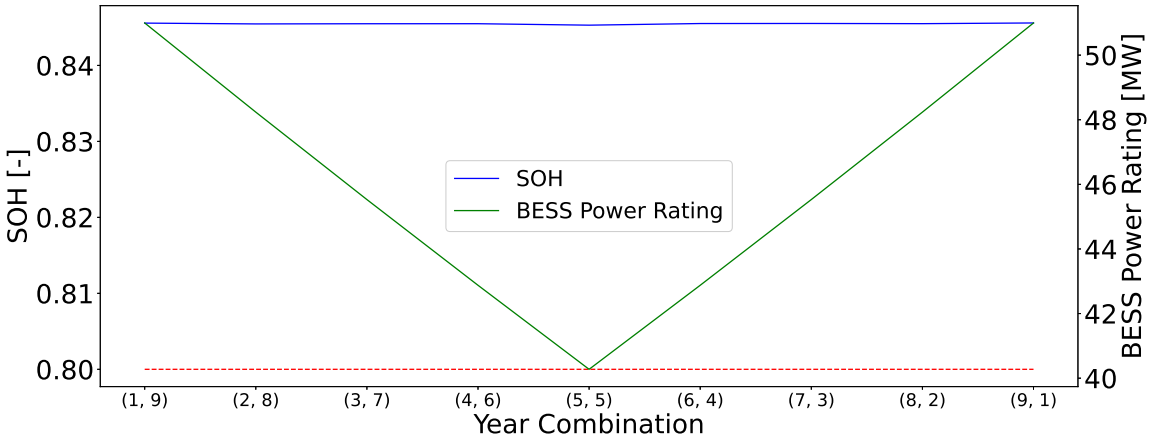

Figure 7.12: Power rating of BESS as a function of the year combination.

BESS capacity. Figures 7.9 and 7.10 can be used as estimation criteria for judging how much BESS capacity needs to be installed based on the acceptable levels of total unserved energy, total unserved energy duration, and acceptable fraction of unserved energy.

Extending the service life of BESS provides for a more economical investment. One schema to increase the service life of BESS while keeping true to the original application is to move the BESS to a different substation where transmission deferral is required. This makes sense provided the load is less than at the original substation. Smaller load will result in increased service life of BESS.

In an example where BESS will be operational for 10 years, and the load increases

at 2% per year, the BESS can be kept at the origin substation for 2 years, and then move it to the target substation and keep it there for 8 years. The BESS will then need to be sized for 8 years of operation, since clearly 8 years of operation with 2% load increase will require higher capacity and power rating. To be clear, we are assuming that the load doesn't grow in the first year, and increases by 2% in the 2nd year. When we move the BESS to the target substation the load at that substation is equivalent to the original load. Then after 1 year at the target substation the load will increase by 2%, and then will increase again in the following year etc.

A curve can be constructed that depicts the final SOH and BESS capacity as a function of the combination of years, such as (1,9), (2,8), ..., (8,2), (9,1). We assume here a load increase of 2% per year. A plot of this for a 10-year period is shown in Figure 7.11. The smallest BESS capacity is at a combination of (5,5) years, with the combinations of (9,1)/(1,9) years yielding BESS capacities much larger. As expected, the BESS capacity increases with the increasing total number of service years. The SOH stays approximately constant with the year combinations, ranging between 0.8452 and 0.8456. The curve of the power rating against the year combinations is shown in Figure 7.12 and, similar to the capacity curve, shows that the power rating of the BESS is minimized for the (5,5) year combination.

If you keep the BESS at the same substation Figure 7.13 shows the total unserved energy of the BESS against its capacity and power rating for a 10-year duration. Unserved energy is calculated as the sum of the unserved energies over the service life. This figure is an extension of Figure 7.9. No unserved energy occurs at capacities greater than 60 MWh and power rating greater than 60 MW. The amount of unserved energy decreases monotonically with increasing BESS capacity and BESS power rating. This curve can be used to choose the BESS capacity and power rating given a feasible region formed around the pre-determined total unserved energy amount. Similarly, Figure 7.14 shows the total duration of unserved energy events against its capacity and power rating for a 10-year time period. No unserved events occur when

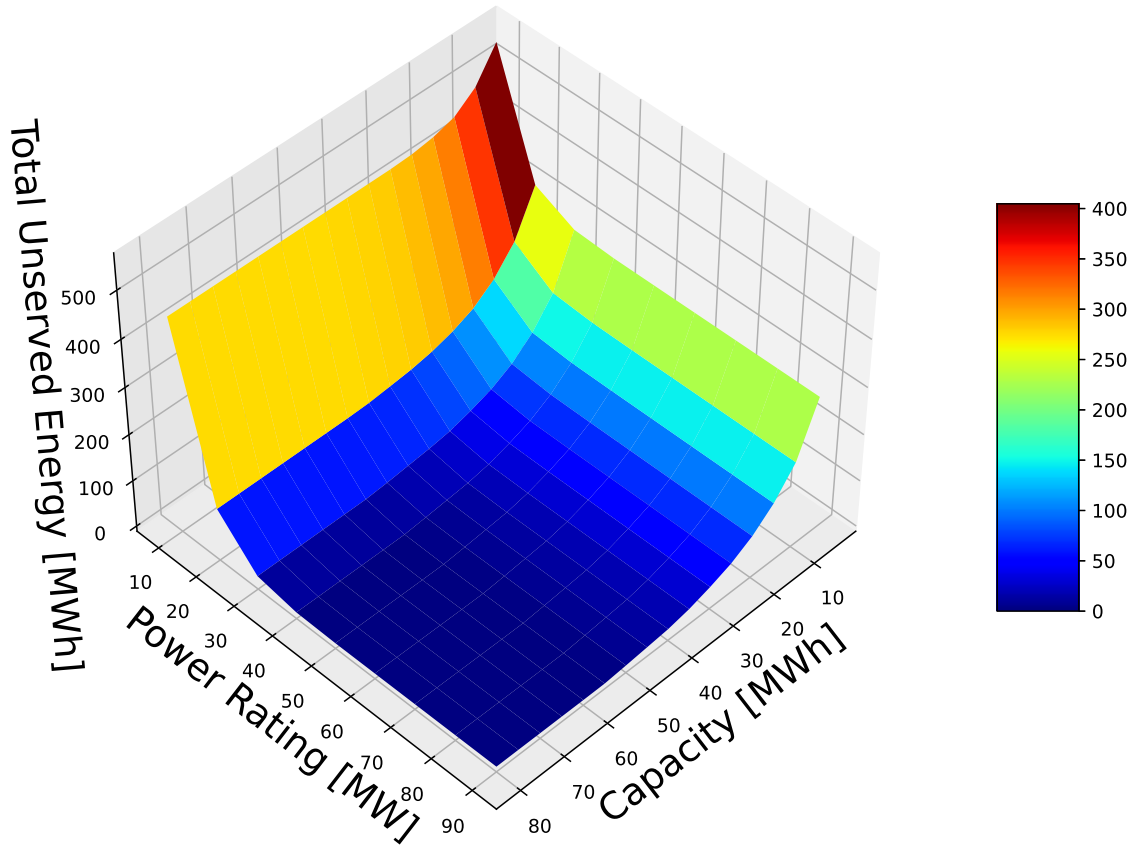

Figure 7.13: Unserved energy of BESS against power rating and BESS capacity.

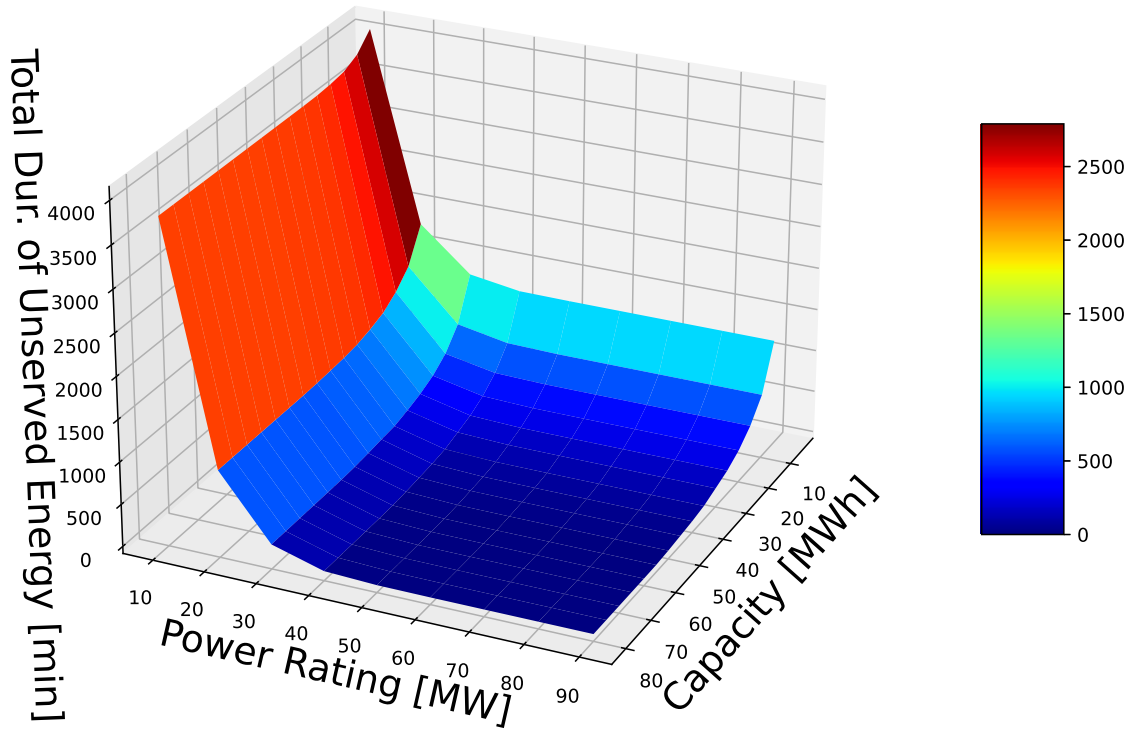

Figure 7.14: Total duration of unserved energy of BESS against power rating and BESS capacity.

the capacity is larger than or equal to 60 MWh and power rating is larger than or equal to 60 MW. The total duration of unserved energy monotonically decreases with increasing BESS capacity and BESS power rating.

7.6 Discussion

We ran grid-search simulations based on 2-bus grid setup shown in Figure 7.1 to calculate the BESS service life, and unserved energy amounts.

Given that a utility would want their BESS to last 10 years, in that time period a 1-hour outage would translate into 600 minutes of total unserved energy events over 10 years, and would also mean 10 events. Given a 100 MW outage, over 10 years this would translate into 1000 MWh of total unserved energy. Keeping these numbers in mind, together with a conservative load increase rate of 2% per year, the transmission utility can use the graphs above to select the BESS capacity, and BESS power rating to suit their needs.

From the Figure 7.2 it is evident that all BESSs considered last more than 10 years and so any BESS greater than 5 MWh in capacity is considered. Examining the graphs showing the load increase of 2% only, from Figure 7.3 it can be deduced that simply running the BESS to 70% SOH instead of 80% SOH will increase the service life of the BESS by around 30%. It can also be observed that no BESSs SOH went as low as 60% for any BESS capacity.

From Figure 7.4 unserved energy at each of the year's end for each of the capacities. For 35 MWh no unserved energy event exceeds 60 minutes in duration, as shown in Figure 7.6. From Figure 7.7 we can see that at 35 MWh BESS capacity we have less than 10 unserved energy events over 10 years.

From Figure 7.9 any BESS capacity above 5 MWh is able to satisfy less than 1000 MWh of total unserved energy requirement, however, while a 10 MWh BESS would last just under 13 years, a 30 MWh BESS, a 3x increase in capacity, would last at least 15 years, a 15% increase in service life, at a higher cost of BESS capacity. From

Figure 7.5 we can observe that a 60 MWh BESS results in unserved energy at 10 years, while a 10 MWh BESS results in unserved energy at just under 2.5 years of operation.

From Figure 7.10, 45 MWh BESS results in less than 600 minutes of total unserved energy duration. From Figure 7.9 for each capacity the fraction of unserved energy to total delivered energy is less than 0.05%, which implies that this metric is irrelevant to the sizing of BESS.

From Figure 7.13 all combinations of capacities and power ratings result in a total unserved energy of less than 1000 MWh. From Figure 7.14 the intersection of the 3-dimensional surface with a plane representing 600 minutes of total unserved energy duration defines a curve the boundaries of which define feasible combinations of power rating and capacities that result in 600 minutes or less of total unserved energy duration. This boundary curve is plotted in Figure 7.16. Capacities larger than or equal to 15 MWh and power ratings larger than or equal to 30 MW result in total duration of unserved energy events equal to and less than 600 minutes, provided the combinations of power rating and capacity lie in the feasible region. Since the highest capacity chosen was 45 MWh and is greater than the 30 MWh capacity calcualted from Figure 7.16 we can chose 30 MW power rating.

When we try to increase the lifetime of the BESS by moving it between the different substations the SOH of the BESS changes insignificantly compared to the changes in BESS capacity and BESS power rating. For a 10-year operation the BESS capacity at (5,5) year combination is just under 15 MWh and power rating is at just under 40 MW. At (9,1)/(1,9) year combinations the BESS capacity is just over 40 MWh and 50 MW, 2.5 times higher in terms of capacity and 25% higher in terms of power rating. This implies keeping the BESS at a certain location and then transferring it to a new location and keeping the BESS there for the equivalent number of years minimizes BESS capacity and power rating. This process is shown in Figure 7.15.

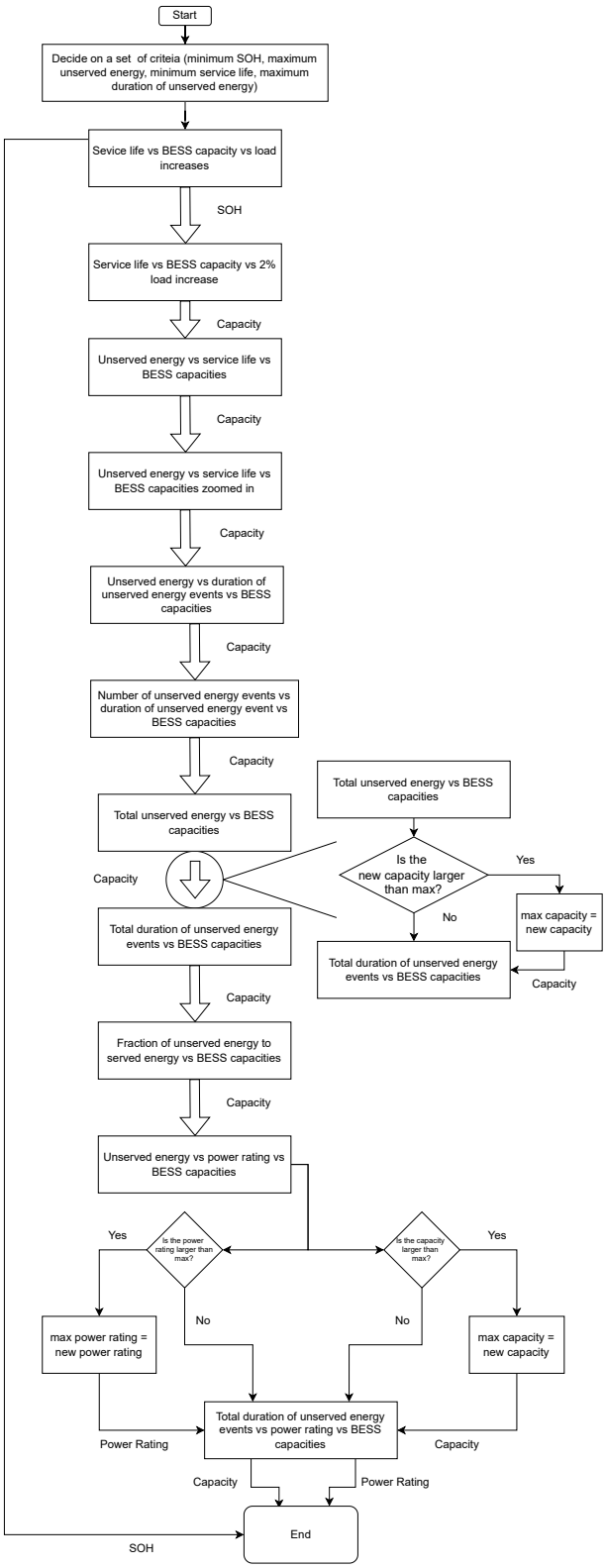

Figure 7.15: Capacity and power rating determination method.

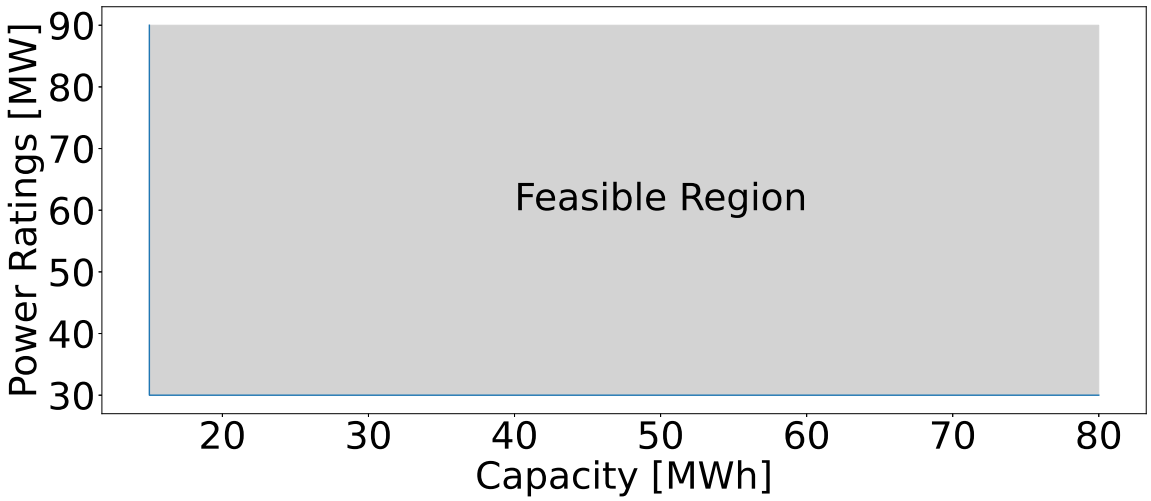

Figure 7.16: Capacity and power rating feasible region.

7.7 Conclusion

We have presented here general methodology for sizing BESS capacity and power rating that takes into account battery degradation, transmission line outages, dynamic line rating, and load growth. The method can be based on non-linear programming or the grid search approach. The method was tested on 2-bus grid setup in Canada. We also presented a BESS capacity sizing evaluation method based on grid search simulations. Future work can include applying a probabilistic approach to sizing and using more accurate BESS degradation methodology. This work can also be extended to calculate the optimal size of each individual BESS at every bus.

Chapter 8

Conclusion

8.1 Summary

The main goal of this thesis was to develop a BESS sizing methodology by combining DTLR and BESS degradation. Once the BESS was sized the main focus of the research was to evaluate the BESS capacity in terms of unserved energy, unserved energy duration, and BESS service life. Another goal of this research was to explore the benefits of load and ampacity forecasting to decentralized BESS control. Deep Reinforcement Learning algorithms were evaluated on the task of operating multiple BESS in a 6-bus RTS.

Objective 1 was addressed by developing a WGAN-based method for creating synthetic data. The method was published in the paper "Generation of Synthetic Ampacity and Electricity Pool Prices using Generative Adversarial Networks." Objective 2 was addressed by creating a BESS sizing methodology based on non-linear programming that takes into account DTLR, transmission line outages, and BESS degradation. This methodology was published in the paper "Sizing Transmission-Scale Battery Energy Storage System with Dynamic Thermal Line Rating." Additionally, objective 2 was fulfilled by creating a method to evaluate the BESS capacity and BESS power rating, by creating graphs of total unserved energy, total unserved energy duration, and service life. This method is to be submitted for publication in a paper "Sizing and Evaluation of Battery Energy Storage System in Transmis-

sion Systems with Dynamic Thermal Line Rating." Objective 3 was accounted for by creating a CNN-biLSTM forecast of model of load and transmissible power, which was then used, in conjunction with a non-linear programming approach, to calculate BESS actions. This work is to be published in a paper "Deep Learning Control of Transmission System with Battery Storage and Dynamic Line Rating." Objective 4 was addressed by applying SAC, DDPG, MASAC, and MADDPG, to a problem of BESS control in an IEEE 6-bus RTS. The findings demonstrated how BESS can be controlled using the SAC actor model and this work is to be submitted in a paper "Deep Reinforcement Learning Operation of Battery Storage with Dynamic Line Rating".

8.2 Contributions

The list of original accomplishments described in this thesis can be summarized as the following:

- Development of a method of creating synthetic 100-step DTLR and Alberta electricity pool price values using Wasserstein GANs for simulation, dataset enhancement, and model training.
- Development of the methodology for BESS sizing in a multi-bus system that takes into account BESS degradation, transmission line outages, and DTLR.
- Development of a method for the determining the length of time, which, when used in a non-linear programming optimization at any time step in the load and ampacity time series, captures the largest BESS capacity needed to alleviate unserved load, provided the BESS is fully charged at the start of the simulation. An approach to increase the BESS capacity to ensure that BESS does not need to be fully charged at the start of the optimization was presented. This length of time was also shown to be the smallest horizon needed to forecast load and ampacity to predict BESS actions using non-linear programming. Performed

an empirical study on the BESS capacity size and BESS Power Rating size when BESS is moved from one substation to another, which helps determine the smallest capacity and power rating of BESS.

- Empirical demonstration of the applicability of multiple single-agent and multi-agent DRL algorithms to the problem of BESS operation that determined that SAC is the superior algorithm when operating multiple BESS in a multi-bus RTS.

8.3 Future Considerations

This work can be extended by looking into the following items:

- Applying other Deep Reinforcement Learning algorithms to the problem of distributed BESS operation, such as Proximal Policy Optimization, and Advantage Actor Critic.
- Extending the BESS sizing methodology to size individual BESS, instead of making the assumptions that all BESSs have the same capacity.
- Applying Genetic Algorithms to the problem of BESS sizing to compare the speed of convergence and accuracy.
- Adding renewable installations, such as wind turbines, or solar plants into the 24-bus RTS and sizing the BESS with them.

Thesis Publication List (as of November 2022)

This section lists the academic contributions made during the course of this masters thesis, including journal papers, conference papers, and patents.

Thesis-Related Publications

This section lists the refereed journals, patents, and conference papers published during the course of this thesis work which are directly related to the thesis objectives.

Conferences

1. Avkhimenia, Vadim, Tim Weis, and Petr Musilek. "Generation of Synthetic Ampacity and Electricity Pool Prices using Generative Adversarial Networks." 2021 IEEE Electrical Power and Energy Conference (EPEC). IEEE, 2021.

2. Avkhimenia, Vadim, Petr Musilek, and Tim Weis. "Sizing Transmission-Scale Battery Energy Storage System with Dynamic Thermal Line Rating." 2022 IEEE Power and Energy Society General Meeting (PES GM). IEEE, 2022.

3. Avkhimenia, Vadim, Matheus Gemignani, Petr Musilek, and Tim Weis. "Deep Learning Control of Transmission System with Battery Storage and Dynamic Line Rating." 2022 IEEE Sustainable Power and Energy Conference (iSPEC). IEEE, 2022 (to be presented).

Journals

1. Avkhimenia, Vadim, Matheus Gemignani, Petr Musilek, and Tim Weis. "Deep Reinforcement Learning Operation of Battery Storage with Dynamic Line Rating." 2022 MDPI Energies.

Bibliography

[1] C. Zhang, S. R. Kuppannagari, R. Kannan, and V. K. Prasanna, "Generative Adversarial Network for Synthetic Time Series Data Generation in Smart Grids," *2018 IEEE International Conference on Communications, Control, and Computing Technologies for Smart Grids, SmartGridComm 2018*, 2018.

[2] D. Hazra and Y. C. Byun, "Synsiggan: Generative adversarial networks for synthetic biomedical signal generation," *Biology*, vol. 9, no. 12, pp. 1–20, 2020.

[3] I. Goodfellow *et al.*, "Generative adversarial nets," *Advances in neural information processing systems*, vol. 27, 2014.

[4] IEEE, "IEEE Standard for Calculating the Current-Temperature Relationship of Bare Overhead Conductors," *IEEE Std 738-2012 (Revision of IEEE Std 738-2006 - Incorporates IEEE Std 738-2012 Cor 1-2013)*, pp. 1–72, 2013.

[5] *Energy Trading System*.

[6] R. S. Sutton and A. G. Barto, *Reinforcement learning: An introduction*. MIT press, 2018.

[7] M. Al-Saffar and P. Musilek, "Reinforcement learning-based distributed bess management for mitigating overvoltage issues in systems with high pv penetration," *IEEE Transactions on Smart Grid*, vol. 11, no. 4, pp. 2980–2994, 2020.

[8] E. Fernandez, I. Albizu, G. Buigues, V. Valverde, A. Etxegarai, and J. G. Olazarri, "Dynamic line rating forecasting based on numerical weather prediction," in *2015 IEEE Eindhoven PowerTech*, IEEE, 2015, pp. 1–6.

[9] A. Mikołajczyk and M. Grochowski, "Data augmentation for improving deep learning in image classification problem," in *2018 international interdisciplinary PhD workshop (IIPhDW)*, IEEE, 2018, pp. 117–122.

[10] C. Hagenboom, "Generation of Synthetic Financial Time-Series with Generative Adversarial Networks," Ph.D. dissertation, Maastricht University, 2020.

[11] S. L. Hyland, C. Esteban, and G. Rätsch, "Real-valued (medical) time series generation with recurrent conditional GANs," *arXiv*, 2017. arXiv: 1706.02633.

[12] S. Harada, H. Hayashi, and S. Uchida, "Biosignal Generation and Latent Variable Analysis with Recurrent Generative Adversarial Networks," *IEEE Access*, vol. 7, pp. 144 292–144 302, 2019. arXiv: 1905.07136.

[13] F. Zhu, F. Ye, Y. Fu, Q. Liu, and B. Shen, "Electrocardiogram generation with a bidirectional LSTM-CNN generative adversarial network," *Scientific Reports*, vol. 9, no. 1, pp. 1–11, 2019.

[14] K. G. Hartmann, R. T. Schirrmeister, and T. Ball, "EEG-GAN: Generative adversarial networks for electroencephalograhic (EEG) brain signals," *arXiv*, 2018. arXiv: 1806.01875.

[15] F. Fahimi, Z. Zhang, W. B. Goh, K. K. Ang, and C. Guan, "Towards EEG generation using gans for bci applications," *2019 IEEE EMBS International Conference on Biomedical and Health Informatics, BHI 2019 - Proceedings*, pp. 2019–2022, 2019.

[16] M. Wiese, R. Knobloch, R. Korn, and P. Kretschmer, "Quant GANs: deep generation of financial time series," *Quantitative Finance*, vol. 20, no. 9, pp. 1419–1440, 2020. arXiv: 1907.06673.

[17] R. Fu, J. Chen, S. Zeng, Y. Zhuang, and A. Sudjianto, "Time Series Simulation by Conditional Generative Adversarial Net," *International Journal of Neural Networks and Advanced Applications*, vol. 7, pp. 1–33, 2020. arXiv: 1904.11419.

[18] J. Yoon, D. Jarrett, and M. van der Schaar, "Time-series generative adversarial networks," *Advances in Neural Information Processing Systems*, vol. 32, no. NeurIPS, pp. 1–11, 2019.

[19] J. Zhang, M. Zhu, and L. Peng, "Customized Parking Data Generation based on Multi-conditional GAN," *2020 IEEE 23rd International Conference on Intelligent Transportation Systems, ITSC 2020*, 2020.

[20] D. Parthasarathy, K. Backstrom, J. Henriksson, and S. Einarsdottir, "Controlled time series generation for automotive software-in-the-loop testing using GANs," *Proceedings - 2020 IEEE International Conference on Artificial Intelligence Testing, AITest 2020*, pp. 39–46, 2020. arXiv: 2002.06611.

[21] M. Arjovsky, S. Chintala, and L. Bottou, "Wasserstein generative adversarial networks," in *International conference on machine learning*, PMLR, 2017, pp. 214–223.

[22] K. Smith and A. O. Smith, "Conditional gan for timeseries generation," *arXiv*, pp. 1–15, 2020. arXiv: 2006.16477.

[23] K. E. Smith and A. O. Smith, "A spectral enabled gan for time series data generation," *arXiv preprint arXiv:2103.01904*, 2021.

[24] H. Ni, L. Szpruch, M. Wiese, S. Liao, and B. Xiao, "Conditional Sig-Wasserstein GANs for Time Series Generation," *SSRN Electronic Journal*, pp. 1–32, 2020. arXiv: 2006.05421.

[25] F. De Meer Pardo, "Enriching Financial Datasets with Generative Adversarial Networks," Ph.D. dissertation, Delft University of Technology, 2019.

[26] Z. Pan, W. Yu, X. Yi, A. Khan, F. Yuan, and Y. Zheng, "Recent Progress on Generative Adversarial Networks (GANs): A Survey," *IEEE Access*, vol. 7, pp. 36 322–36 333, 2019.

[27] Y. LeCun, L. Bottou, Y. Bengio, and P. Haffner, "Gradient-based learning applied to document recognition," *Proceedings of the IEEE*, vol. 86, no. 11, pp. 2278–2324, 1998.

[28] F. Chollet *et al.*, *Keras*, https://keras.io, 2015.

[29] J. Brownlee, *How to Develop a Wasserstein Generative Adversarial Network (WGAN) From Scratch*.

[30] H. K. Nguyen, J. B. Song, and Z. Han, "Demand side management to reduce peak-to-average ratio using game theory in smart grid," in *2012 Proceedings IEEE INFOCOM Workshops*, IEEE, 2012, pp. 91–96.

[31] B. Keyvani, M. Power, and D. Flynn, "Enhancing network utilisation in wind-rich regions using coordinated dynamic line rating, energy storage and power flow control schemes," in *The 9th Renewable Power Generation Conference (RPG Dublin Online 2021)*, vol. 2021, 2021, pp. 324–329.

[32] S. Karimi, P. Musilek, and A. M. Knight, "Dynamic thermal rating of transmission lines: A review," *Renewable and Sustainable Energy Reviews*, vol. 91, pp. 600–612, 2018.

[33] T. Barton, M. Musilek, and P. Musilek, "The effect of temporal discretization on dynamic thermal line rating," in *2020 21st International Scientific Conference on Electric Power Engineering (EPE)*, IEEE, 2020, pp. 1–6.

[34] H. Mehrjerdi, E. Rakhshani, and A. Iqbal, "Substation expansion deferral by multi-objective battery storage scheduling ensuring minimum cost," *Journal of energy storage*, vol. 27, p. 101 119, 2020.

[35] D. Werner, S. Paarmann, and T. Wetzel, "Calendar aging of li-ion cells—experimental investigation and empirical correlation," *Batteries*, vol. 7, no. 2, p. 28, 2021.

[36] I. Goodfellow, Y. Bengio, and A. Courville, *Deep Learning*. MIT Press, 2016, http://www.deeplearningbook.org.

[37] H. C. Hesse, R. Martins, P. Musilek, M. Naumann, C. N. Truong, and A. Jossen, "Economic optimization of component sizing for residential battery storage systems," *Energies*, vol. 10, no. 7, p. 835, 2017.

[38] R. Martins, H. C. Hesse, J. Jungbauer, T. Vorbuchner, and P. Musilek, "Optimal component sizing for peak shaving in battery energy storage system for industrial applications," *Energies*, vol. 11, no. 8, p. 2048, 2018.

[39] R. Martins, P. Musilek, H. C. Hesse, J. Jungbauer, T. Vorbuchner, and A. Jossen, "Linear battery aging model for industrial peak shaving applications," in *2018 IEEE International Conference on Environment and Electrical Engineering and 2018 IEEE Industrial and Commercial Power Systems Europe (EEEIC/I&CPS Europe)*, IEEE, 2018, pp. 1–6.

[40] M. K. Metwaly and J. Teh, "Optimum network ageing and battery sizing for improved wind penetration and reliability," *IEEE Access*, vol. 8, pp. 118 603–118 611, 2020.

[41] M. K. Metwaly and J. Teh, "Probabilistic peak demand matching by battery energy storage alongside dynamic thermal ratings and demand response for enhanced network reliability," *IEEE Access*, vol. 8, pp. 181 547–181 559, 2020.

[42] A. Hussain, V.-H. Bui, and H.-M. Kim, "Impact analysis of demand response intensity and energy storage size on operation of networked microgrids," *Energies*, vol. 10, no. 7, p. 882, 2017.

[43] E. I. Vrettos and S. A. Papathanassiou, "Operating policy and optimal sizing of a high penetration res-bess system for small isolated grids," *IEEE Transactions on Energy Conversion*, vol. 26, no. 3, pp. 744–756, 2011.

[44] U. Mulleriyawage and W. Shen, "Impact of demand side management on optimal sizing of residential battery energy storage system," *Renewable Energy*, vol. 172, pp. 1250–1266, 2021.

[45] D. Mejía-Giraldo, G. Velásquez-Gomez, N. Muñoz-Galeano, J. B. Cano-Quintero, and S. Lemos-Cano, "A bess sizing strategy for primary frequency regulation support of solar photovoltaic plants," *Energies*, vol. 12, no. 2, p. 317, 2019.

[46] M. Galeela, "Reliability evaluation of electric power systems integrating smart grid solutions," Ph.D. dissertation, University of Manchester, 2019.

[47] M Abogaleela and K Kopsidas, "Battery energy storage degradation impact on network reliability and wind energy curtailments," in *2019 IEEE Milan PowerTech*, IEEE, 2019, pp. 1–6.

[48] *British atmospheric data center (badc)*.

[49] Subcommittee, Probability Methods, "IEEE reliability test system," *IEEE Transactions on power apparatus and systems*, no. 6, pp. 2047–2054, 1979.

[50] IEEE, "IEEE standard for calculating the current-temperature relationship of bare overhead conductors," *IEEE Std 738-2012 (Revision of IEEE Std 738-2006 - Incorporates IEEE Std 738-2012 Cor 1-2013)*, pp. 1–72, 2013.

[51] Gurobi Optimization, LLC, *Gurobi Optimizer Reference Manual*, 2021.

[52] T. Aziz, N.-A. Masood, S. R. Deeba, W. Tushar, and C. Yuen, "A methodology to prevent cascading contingencies using bess in a renewable integrated microgrid," *International Journal of Electrical Power & Energy Systems*, vol. 110, pp. 737–746, 2019.

[53] J. Faraji, A. Ketabi, H. Hashemi-Dezaki, M. Shafie-Khah, and J. P. Catalao, "Optimal day-ahead scheduling and operation of the prosumer by considering corrective actions based on very short-term load forecasting," *IEEE Access*, vol. 8, pp. 83 561–83 582, 2020.

[54] A. Al Mamun, M. Sohel, N. Mohammad, M. S. H. Sunny, D. R. Dipta, and E. Hossain, "A comprehensive review of the load forecasting techniques using single and hybrid predictive models," *IEEE Access*, vol. 8, pp. 134 911–134 939, 2020.

[55] D. A. Douglass *et al.*, "A review of dynamic thermal line rating methods with forecasting," *IEEE Transactions on Power Delivery*, vol. 34, no. 6, pp. 2100–2109, 2019.

[56] E. Reihani, S. Sepasi, L. R. Roose, and M. Matsuura, "Energy management at the distribution grid using a battery energy storage system (bess)," *International Journal of Electrical Power & Energy Systems*, vol. 77, pp. 337–344, 2016.

[57] Y. Zheng *et al.*, "Optimal operation of battery energy storage system considering distribution system uncertainty," *IEEE Transactions on Sustainable Energy*, vol. 9, no. 3, pp. 1051–1060, 2017.

[58] S. Chapaloglou *et al.*, "Smart energy management algorithm for load smoothing and peak shaving based on load forecasting of an island's power system," *Applied energy*, vol. 238, pp. 627–642, 2019.

[59] J. Xiong, P. Zhou, A. Chen, and Y. Zhang, "Attention-based neural load forecasting: A dynamic feature selection approach," in *2021 IEEE Power & Energy Society General Meeting (PESGM)*, IEEE, 2021, pp. 01–05.

[60] L. Sehovac and K. Grolinger, "Deep learning for load forecasting: Sequence to sequence recurrent neural networks with attention," *IEEE Access*, vol. 8, pp. 36 411–36 426, 2020.

[61] J. Lin, J. Ma, J. Zhu, and Y. Cui, "Short-term load forecasting based on lstm networks considering attention mechanism," *International Journal of Electrical Power & Energy Systems*, vol. 137, p. 107 818, 2022.

[62] M. Schuster and K. K. Paliwal, "Bidirectional recurrent neural networks," *IEEE transactions on Signal Processing*, vol. 45, no. 11, pp. 2673–2681, 1997.

[63] B. Lim and S. Zohren, "Time-series forecasting with deep learning: A survey," *Philosophical Transactions of the Royal Society A*, vol. 379, no. 2194, p. 20 200 209, 2021.

[64] I. Sutskever, O. Vinyals, and Q. V. Le, "Sequence to sequence learning with neural networks," *Advances in neural information processing systems*, vol. 27, 2014.

[65] Z. Wang, L. Jia, and C. Ren, "Attention-bidirectional lstm based short term power load forecasting," in *2021 Power System and Green Energy Conference (PSGEC)*, IEEE, 2021, pp. 171–175.

[66] D. Bahdanau, J. Chorowski, D. Serdyuk, P. Brakel, and Y. Bengio, "End-to-end attention-based large vocabulary speech recognition," in *2016 IEEE international conference on acoustics, speech and signal processing (ICASSP)*, IEEE, 2016, pp. 4945–4949.

[67] A. Hussain, V.-H. Bui, and H.-M. Kim, "Deep reinforcement learning-based operation of fast charging stations coupled with energy storage system," *Electric Power Systems Research*, vol. 210, p. 108 087, 2022.

[68] D. Cao *et al.*, "Reinforcement learning and its applications in modern power and energy systems: A review," *Journal of modern power systems and clean energy*, vol. 8, no. 6, pp. 1029–1042, 2020.

[69] B. Zhang *et al.*, "Soft actor-critic–based multi-objective optimized energy conversion and management strategy for integrated energy systems with renewable energy," *Energy Conversion and Management*, vol. 243, p. 114 381, 2021.

[70] J. Khalid, M. A. Ramli, M. S. Khan, and T. Hidayat, "Efficient load frequency control of renewable integrated power system: A twin delayed ddpg-based deep reinforcement learning approach," *IEEE Access*, vol. 10, pp. 51 561–51 574, 2022.

[71] S. Zhang, D. May, M. Gül, and P. Musilek, "Reinforcement learning-driven local transactive energy market for distributed energy resources," *Energy and AI*, vol. 8, p. 100 150, 2022.

[72] T. P. Lillicrap *et al.*, "Continuous control with deep reinforcement learning," *arXiv preprint arXiv:1509.02971*, 2015.

[73] R. Lowe, Y. I. Wu, A. Tamar, J. Harb, O. Pieter Abbeel, and I. Mordatch, "Multi-agent actor-critic for mixed cooperative-competitive environments," *Advances in neural information processing systems*, vol. 30, 2017.

[74] T. Haarnoja, A. Zhou, P. Abbeel, and S. Levine, "Soft actor-critic: Off-policy maximum entropy deep reinforcement learning with a stochastic actor," in *International conference on machine learning*, PMLR, 2018, pp. 1861–1870.

[75] D. Cao *et al.*, "Data-driven multi-agent deep reinforcement learning for distribution system decentralized voltage control with high penetration of pvs," *IEEE Transactions on Smart Grid*, vol. 12, no. 5, pp. 4137–4150, 2021.

[76] D. Cao, W. Hu, J. Zhao, Q. Huang, Z. Chen, and F. Blaabjerg, "A multi-agent deep reinforcement learning based voltage regulation using coordinated pv inverters," *IEEE Transactions on Power Systems*, vol. 35, no. 5, pp. 4120–4123, 2020.

[77] M. Faheem *et al.*, "Smart grid communication and information technologies in the perspective of industry 4.0: Opportunities and challenges," *Computer Science Review*, vol. 30, pp. 1–30, 2018.

[78] A. J. Wood, B. F. Wollenberg, and G. B. Sheblé, *Power generation, operation, and control*. John Wiley & Sons, 2013.

[79] S. Fujimoto, H. Hoof, and D. Meger, "Addressing function approximation error in actor-critic methods," in *International conference on machine learning*, PMLR, 2018, pp. 1587–1596.

[80] G. S. Misyris, A. Venzke, and S. Chatzivasileiadis, "Physics-informed neural networks for power systems," in *2020 IEEE Power & Energy Society General Meeting (PESGM)*, IEEE, 2020, pp. 1–5.

[81] Z. Yan, Y. Xu, Y. Wang, and X. Feng, "Data-driven economic control of battery energy storage system considering battery degradation," in *2019 9th International Conference on Power and Energy Systems (ICPES)*, IEEE, 2019, pp. 1–5.

[82] S. Zhang, S. Nandakumar, Q. Pan, E. Yang, R. Migne, and L. Subramanian, "Benchmarking reinforcement learning algorithms on island microgrid energy management," in *2021 IEEE PES Innovative Smart Grid Technologies-Asia (ISGT Asia)*, IEEE, 2021, pp. 1–5.

[83] V.-H. Bui, A. Hussain, and H.-M. Kim, "Double deep Q-learning-based distributed operation of battery energy storage system considering uncertainties," *IEEE Transactions on Smart Grid*, vol. 11, no. 1, pp. 457–469, 2019.

[84] J. Teh and C.-M. Lai, "Reliability impacts of the dynamic thermal rating and battery energy storage systems on wind-integrated power networks," *Sustainable Energy, Grids and Networks*, vol. 20, p. 100 268, 2019.

[85] J. Teh *et al.*, "Prospects of using the dynamic thermal rating system for reliable electrical networks: A review," *IEEE Access*, vol. 6, pp. 26 765–26 778, 2018.

[86] Y. Liu, X. Wu, J. Du, Z. Song, and G. Wu, "Optimal sizing of a wind-energy storage system considering battery life," *Renewable Energy*, vol. 147, pp. 2470–2483, 2020.

[87] J.-T. Liao, Y.-S. Chuang, H.-T. Yang, and M.-S. Tsai, "Bess-sizing optimization for solar pv system integration in distribution grid," *IFAC-PapersOnLine*, vol. 51, no. 28, pp. 85–90, 2018.

[88] L. A. Wong, V. K. Ramachandaramurthy, S. L. Walker, P. Taylor, and M. J. Sanjari, "Optimal placement and sizing of battery energy storage system for losses reduction using whale optimization algorithm," *Journal of Energy Storage*, vol. 26, p. 100 892, 2019.

[89] Y. Alhumaid, K. Khan, F. Alismail, and M. Khalid, "Multi-input nonlinear programming based deterministic optimization framework for evaluating microgrids with optimal renewable-storage energy mix," *Sustainability*, vol. 13, no. 11, p. 5878, 2021.

[90] P. Boonluk, A. Siritaratiwat, P. Fuangfoo, and S. Khunkitti, "Optimal siting and sizing of battery energy storage systems for distribution network of distribution system operators," *Batteries*, vol. 6, no. 4, p. 56, 2020.